ABSTRACT

Title of Thesis: INVESTIGATION OF PERFORMANCE DEGRADATION OF EVAPORATOR FOR LOW TEMPERATURE REFRIGERATION APPLICATIONS

Jan Muehlbauer, Master of Science, 2006

Thesis Directed By: Professor Reinhard Radermacher, Ph.D.
Department of Mechanical Engineering

An evaporator test stand has been designed, sized, constructed, calibrated and operated to investigate the evaporator performance degradation for low temperature refrigeration applications. Measurements have been taken of air- and refrigerant-side temperatures, refrigerant-side pressures, air- and refrigerant-side differential pressures, air- and refrigerant-side mass flow rate and the power consumption of the electric defrost heater. The system is designed to work as a commercial refrigeration system for low temperature applications including freezing and defrost cycles. A manual and automatic defrost control has been designed and tested. The calculated values are the air- and refrigerant-side capacities. The tests have shown that the system is able to accomplish all desired test conditions.

The performance of the evaporator was evaluated continuously during testing. Its performance degraded constantly by accumulation of frost during each frosting cycle, which resulted in the loss of superheat towards the end of each cycle. The defrost operation could not restore the full capacity of the evaporator. The defrost cycle consists out of two phases, melting the ice and re-cooling the coil. The first phase melts all the ice of the coil but the drainage of the resulting water is incomplete. The re-cooling phase freezes the amount of water residue on the evaporator coil, which causes an accelerated frost formation in the following freezing cycle. All over this behavior causes an accelerated reduction in evaporator capacity and therefore earlier superheat loss. It has been investigated for two air flow rates. The comparison of cycles with different air flow rates showed that with an increased air flow rate the frost density increases and the free flow area of the air passage in the evaporator decreases more slowly.

INVESTIGATION OF PERFORMANCE DEGRADATION OF EVAPORATOR FOR LOW TEMPERATURE REFRIGERATION APPLICATIONS

By

Jan Muehlbauer

Thesis submitted to the Faculty of the Graduate School of the
University of Maryland, College Park, in partial fulfillment
of the requirements for the degree of
Master of Science
2006

Advisory Committee:
Professor Reinhard Radermacher, Chair/Advisor
Assistant Professor Elias Balaras
Assistant Professor Bao Yang

DEDICATION

Dedicated to my parents & Kai

ACKNOWLEDGEMENT

I would like to thank Prof. Dr. Reinhard Radermacher, Director of CEEE, for giving me the opportunity to accomplish my Master of Science at the University of Maryland. Also Dr. Hwang, who guided and helped me through my work.

I thank all other faculty, staff and students at CEEE. Special thanks also goes to the experimental group members, Ahmet Ors, Xudong Wang, Mr. Jin, Cara Sanderson, John Linde, Amr Gado and Dr. Jun for the great teamwork and the enjoyable atmosphere in our lab.

Finally, I would like to thank my parents, my sister and all my extended family and friends, either here or back home, for their great support.

Table of Content

List of Tables

List of Figures

Nomenclature

D_h	Hydraulic Diameter	[m]
Re	Reynolds Number	[-]
V, v	Velocity	[m/s]
V_{dis}	Displacement Volume	[m^3]
f, f'	Friction Factor	[-]
P	Pressure	[kPa]
ΔP	Differential Pressure	[Pa]
L	Length	[m]
C_d	Nozzle Friction Loss Correction Factor	[-]
A, a	Area	[m^2]
D, d	Diameter	[m]
w, m	Mass Flow Rate	[kg/s]
T	Temperature	[°C]
ΔT	Temperature Difference	[°C]
W_{comp}	Compressor Power Consumption	[W]
RH	Relative Humidity	[%]
error	Error	[%]
h	Enthalpy	[kJ/kg]
s	Entropy	[kJ/kg K]
Q	Capacity	[W]
Q_{heater}	Power consumption of the heater	[W]
g	Gravitational Constant	[m/s^2]
h_1, h_2	Height	[m]
c_p	Specific heat capacity at constant pressure	[kJ/kg K]

RPM	Revolution per minute	[1/min]
humRat	Humidity Ratio	[g/kg]
U	Overall heat transfer Coefficient	[W/m^2 K]
Nu	Nusselt Number	[-]
Pr	Prandtl Number	[-]
k_f	Thermal Conductivity	[W/m K]

Greek

ν	Kinematic Viscosity	[m^2/s]
ε	Roughness Factor	[m]
ρ	Density	[kg/m^3]
β	Geometry coefficient	[-]
η	Efficiency	[-]
α	Thermal Diffusivity	[W/m K]
δ_w	Wall Thickness	[m]

Subscripts

isen	Isentropic
comp	Compressor
vol	Volumetric
dis	Displacement
evap; ev	Evaporator
in	Inlet

out	Outlet
exp	Expansion Valve
cond	Condenser
sat	Saturated
sup	Superheat
sub	Subcool
hx	Heat Exchanger
f	Fluid
lam	Laminar
turb	Turbulent

1 Introduction

Low temperature refrigeration, at temperatures below 0°C, affects everyday life. It is mostly used for food preservation, such as in the freezer of a refrigerator. There are different kinds of refrigeration systems according to different refrigeration temperatures. For low temperature refrigeration with temperature above -20°C, single-stage refrigeration systems are used, below -20°C, two-stage systems or compound systems are used. The primary refrigerant for these systems is R-22. However, R-22 will be phased out due to environmental issues. A proposed replacement is R-404A.

When the temperature is lower than the freezing point of water, formation of frost occurs. Frost, like snow, is the result of deposition of water vapor in saturated air. The difference between snow and ice is that snow is formed from a transformation of water vapor into solid state, however, when water vapor condense and then solidifies, ice or sleet is formed. Figure 1, a morphological diagram, shows different shapes of snow crystals under different temperature and super saturation condition.

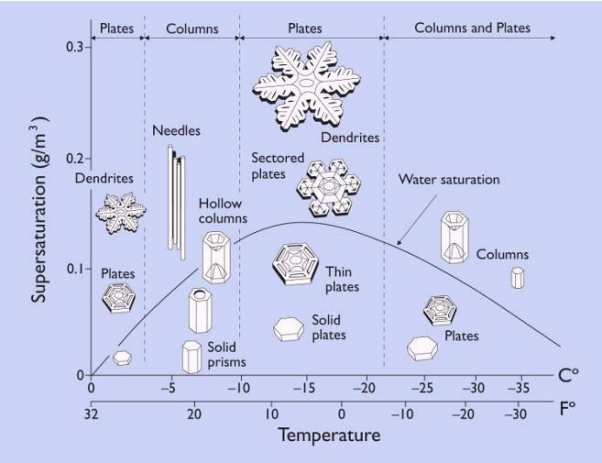

Figure 1: Morphology Diagram [1]

Frost growth on a solid surface happens when the solid surface is colder than the freezing point of water. Frost deposition is formed by condensed and solidified water vapor on the cold surface. Condensation and frost formation start first at various nucleation sites depending on the solid surface. From there it will spread out all over the solid object.

Frost growth can be observed on low temperature evaporators. The evaporator in the refrigeration system provides the coldest surface for condensation of the water vapor and freezing. The frost growth on the evaporator results in decrease of water contend and humidity ratio of air. The initial humidity level determines how much frost can be formed on a coil. Ideally the low temperature chamber should be completely sealed so that after the first frost has been defrosted from the coil the humidity level in the refrigerated space is low enough that no more frost can form. In supermarket application, freezer doors are opened and closed frequently. Every time, when a door opens, it provides the refrigerated space with additional water vapor, which will freeze on the heat exchanger eventually. The frost has a positive and a negative effect. The initial frost will create turbulences in the air flow, which has a positive effect for the heat transfer. However, if the frost growth continues, it causes additional thermal resistance and increases the hydraulic resistance to the air flow, then the capacity of the evaporator will decrease dramatically.

Therefore it is important to investigate the frost formation on heat exchangers especially for low temperature applications in order to understand the effect of frost formation on the performance degradation. Typically, a fin-and-tube type heat exchanger is used for low temperature conditions. The fin spacing is much larger than for medium

temperature heat exchangers to prevent a total block of the air passage by frost. The fin itself usually is flat and polished.

Although frost is a constant problem for low temperature applications, no complete model has been developed to predict it accurately yet. There are too many variables influencing the growth of frost.

2 Literature Review

Many studies have been conducted in attempts to investigate and model frost properties and frosting behavior.

N.H. Fletcher [2] characterized frost formation on a cold surface into two processes: nucleation and crystal growth. The initial frost forms through nucleation on the surface. From this state the ice crystal starts to grow. B. Na et al. [3] investigated the fundamental understanding of factors affecting frost nucleation. He related the surface energy with frost formation. The development of low energy surfaces could lead to less frost. Gibbs Energy is used to describe the energy level of the surface. Most studies do not consider frost nucleation.

Frost growth and frost properties models for a cold flat surface have been developed by R. Yun et al. [4]. Besides a physical model for the frost layer growth and frost properties, an empirical correlation for average frost roughness was presented. Frost roughness is defined as the difference between the height of hill and valley of the frost. The effects of frost roughness and turbulent boundary layer thickness are used to generate a model for heat and mass transfer coefficients.

Above studies were conducted on the fundamentals of frost formation or frost formation on simple geometries like a flat plate. More complex geometries are the next step to use the gained basic knowledge and to create new models. D. Seker et al. modeled [5] and experimentally investigated the frost formation on fin-and-tube type heat exchangers [6]. The model used six main assumptions in order to be able to create a transient semi-empirical model to predict frost growth on forced convection evaporators in domestic refrigerators. The model validation was done experimentally, but there are

still big differences in between the experimental and simulated data, which leaves space for improvement.

Several approaches have been done to create empirical models for frost prediction. Y. Xia et al. [7] presented an empirical study of frost accumulation effects on performance of louvered-fin microchannel heat exchangers. The outcome is that the bridging of the louver gaps by frost is the major reason for a decreased air side heat transfer and therefore a capacity reduction of the coil.

Another approach to deal with frost formation is to reduce the effect of frost growth by surface changes. H. Lee et al. [8] investigated the effect of different surface hydrophilicity. The outcome is frost maps which show what kinds of frost structure will build up on either hydrophobic or hydrophilic surface under specific conditions. Mainly three frost structures are classified: feather type, grass type and plate type. Z. Liu et al. introduced a new anti frosting paint and evaluated it by direct comparison with an uncoated metallic surface [9] and a long term performance test [10]. The paint is based on the theory of Na et al. [3] of a low energy surface. The direct comparison showed that the paint can both efficiently delay the frost crystal nucleation and decrease the frost deposition rate. The long term performance test showed that the surface has frost formation like on a hydrophobic surface with frost of a very lose, weak and fragile structure. Even after more than 2 months of testing a degradation of the anti frost performance of the coating was not observed.

The frost model to predict frost growth on complex geometries, such as complete heat exchangers for any kind of low temperature refrigeration applications, has not been found yet. It seems like that we are far from there.

Although new approaches are conducted to reduce frost formation, it is not possible to avoid frost formation. Therefore an investigation of frost formation characteristic in the actual heat exchanger and its effect on the refrigeration performance is necessary.

3 Objectives

The literature review showed that a considerable amount of research has been conducted relating to frost formation. Simple geometries and different surfaces have been investigated. Many studies on more complex heat exchangers have been conducted only with single phase refrigerant not with two-phase refrigerants.

In order to be able to evaluate the performance a market ready evaporator under real operating conditions tests have to be conducted. Therefore, the current study requires a test facility to experimentally determine the performance degradation of frost formation on heat exchangers. The facility needs to be flexible enough to change the evaporator coils easily to investigate the effect of different fin geometries, heat exchanger types, such as microchannel or spine type. And it has to be as close to a real case refrigeration application as possible. Therefore, the refrigerant in the evaporator has to be a two-phase refrigerant.

It is the objective of this study to investigate the frost formation characteristics of the low temperature evaporator coil and its effect on the refrigeration performance under cyclic operation including freezing and defrosting processes.

4 Test Facility

The test facility must simulate realistic operating conditions for low temperature applications. Small capacity low temperature refrigeration systems, such as a reach-in unit, are commonly used in supermarkets and small stores to keep food frozen. For a reach-in unit the refrigerated space is at a low temperature and the condensing unit is exposed to an ambient condition. For this reason, a wind tunnel containing the evaporator was built in an environmental chamber that has the capacity to go down to -40ºC. The condensing unit was installed in a separate climate chamber to simulate outdoor conditions.

4.1 Test Heat Exchanger

The heat exchanger for the test is a standard fin-and-tube type heat exchanger. It is commercially available for reach-in units. Its specifications are shown in Table 1.

Table 1: Test Evaporator Specifications

Dim	W × H × D [in(m)]	21 5/16×4×7 (0.54×0.10×0.18)
	Frontal Area[ft²(m²)]	0.592 (0.055)
Fin	Shape	plate fin
	No. of Fins	149 (7 FPI)
	Thickness [in (mm)]	0.002(0.05)
Tube	Step Pitch [mm]	25.5
	Row Pitch [mm]	25.5
	No. of Row	7
	No. of Tubes per Row	4
	Tube Diameter [in(mm)]	3/8 (9.525)
	No. of Circuit	1→2→1
	Tube Shape	Round
Heat Transfer Area (m²)		4.805

The circuitry of the heat exchanger has a special design. To begin, one tube enters the coil, then after the first row, the tube splits up into two rows which combine at the outlet back to one tube. The design is shown in Figure 2.

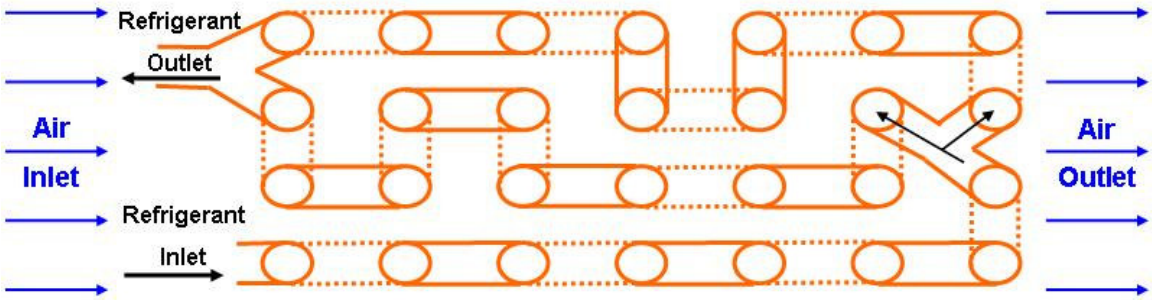

Figure 2: Circuitry of Test Heat Exchanger

Since the test will include frost formation, it is necessary to defrost the heat exchanger. This is done by an electric heater, which is directly installed onto the fins of the bottom side of the heat exchanger. The left picture in Figure 3 shows the coil with the electric defrost heater. In the same picture, there are two temperature switches at the outlet of the evaporator which are wired to a control box. They will be used to determine the two phases of the defrost cycle, the electric heater defrost and the re-cooling the coil.

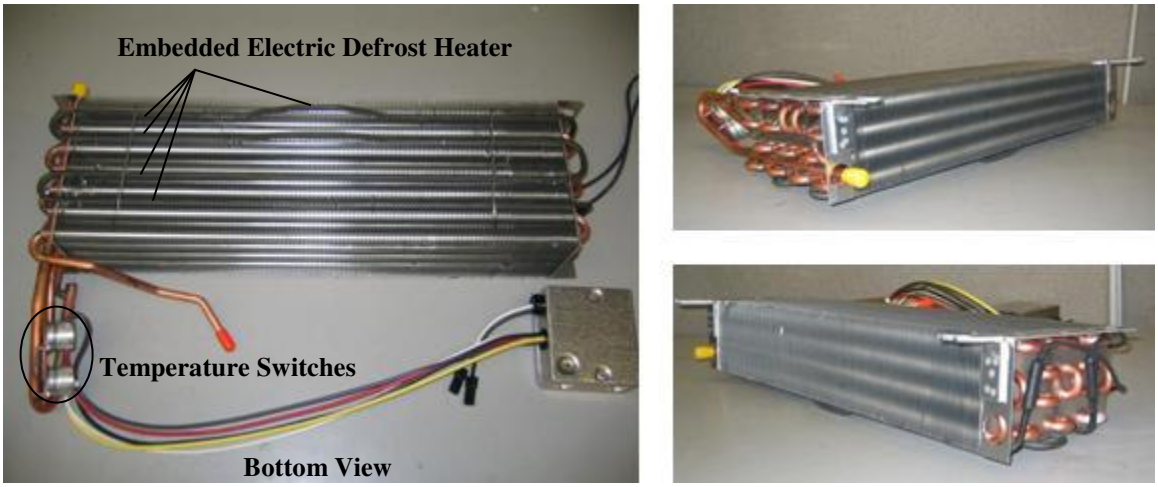

Figure 3: Pictures of Test Heat Exchanger

4.2 Test Conditions

Frost plays an important role in low temperature applications. The test conditions were established to determine the effects of frost formation on the performance of the heat exchanger. The relative humidity, in particular, plays an important role in the experimental set-up, as well as for the test conditions.

Table 2: Test Conditions - Refrigerant side

Evaporation Temperature	-10 °F	-23.3 °C
Refrigerant vapor temperature	-2 °F	-18.9 °C
Degree of Superheating	8 °F	4.5 °C
Condensing Temperature	110 °F	43.3 °C
Liquid refrigerant temperature	95 °F	35 °C
Degree of Subcooling	15 °F	8.3 °C

Table 2 shows the test conditions for the refrigeration circuit and Table 3 shows the conditions for the air inlet temperature of the evaporator. The refrigerant R22 was used for all tests.

Table 3: Test Conditions - Air side

Air Inlet Temperature	0 °F	-17.8 °C
Air Flow Rate	210 ft^3/min 240 ft^3/min	0.099 m^3/s 0.113 m^3/s
RH		80%

R22 is still a widely used refrigerant, and based on the evaporation and condensing temperature, the expected refrigeration cycle can be visualized in a pressure-enthalpy diagram. This is shown in Figure 4, assuming isenthalpic expansion and isentropic compression.

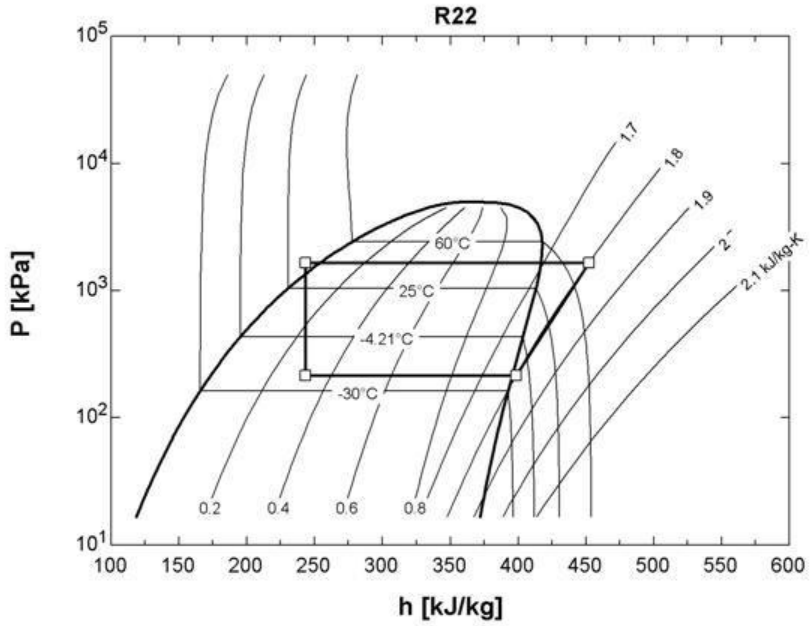

Figure 4: Expected Refrigeration Cycle in p-h Diagram

4.3 Wind Tunnel Layout / Design

In order to adequately test a heat exchanger, it is necessary to place it into a wind tunnel. The wind tunnel can be a part of a controlled closed loop or an open wind tunnel installed in an environmental chamber. In both cases, it is important that the inlet conditions for the test heat exchanger are controlled. There are several advantages for using an open wind tunnel. It is easily accessible, more flexible in terms of placement and size, and easier to change, repair and manufacture. Only environmental chambers are

necessary to conduct the tests. Consequently, the heat exchanger test facility consists of an open wind tunnel integrated with the test evaporator and a condensing unit, each of which is placed in a different environmental chamber. Figure 5 shows the system layout. The bold framing lines indicate the environmental chamber walls. The refrigeration system is designed to be controlled from only the condensing unit chamber so that the evaporator air condition will not be affected during the test.

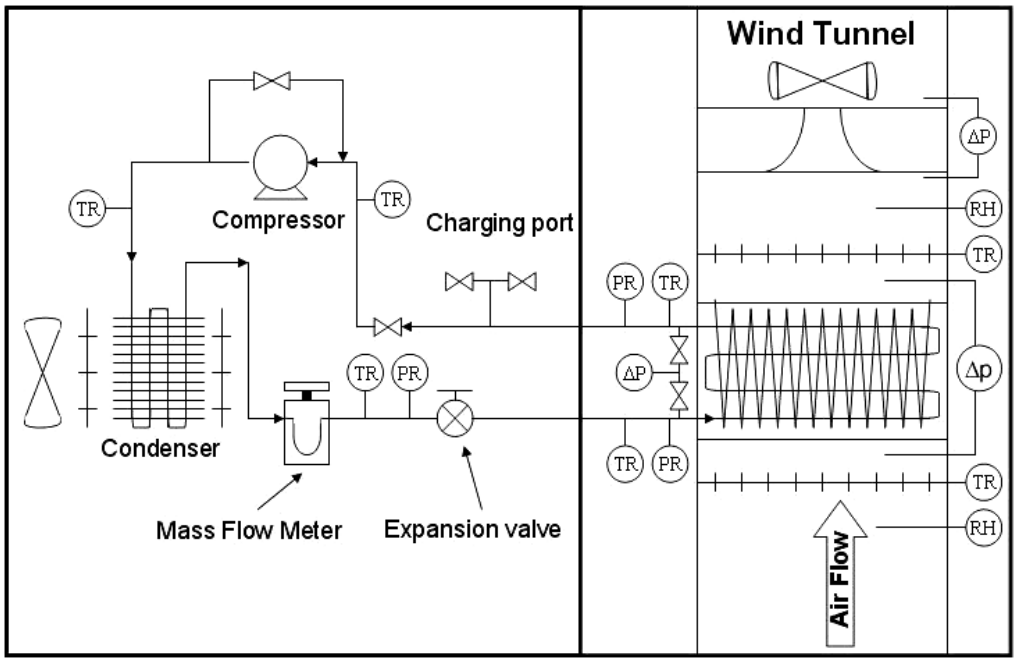

Figure 5: System Layout

As shown in Figure 5, the majority of measurements are taken at the evaporator. In order to calculate the airside capacity, two thermocouple grids and a relative humidity sensor were installed at the inlet of the evaporator and four thermocouple grids consisting out of two thermocouples each and a relative humidity sensor were installed at the outlet. To determine the air mass flow rate, a standard ASME long radius nozzle with 3" throat diameter was installed. The differential pressure and temperature across the nozzle were measured in order to calculate the air mass flow rate through the duct and evaporator.

The pressure drop across the evaporator was also measured, which is an indicator for frost growth.

For the refrigerant side it is important to determine the inlet and outlet conditions of the evaporator as well as the refrigerant mass flow rate. The inlet and outlet conditions are needed to determine the enthalpies, which in connection with the mass flow rate are used to calculate the refrigeration capacity. When comparing different types of evaporators, it is important to have a refrigerant side differential pressure transducer across the heat exchanger. A complete list of all measurements is shown in Table 4.

Table 4: System Measurements

Air-Side	**Ref.-Side**
Evaporator Inlet Temp. (2 x 4 T/C)	Inlet Temp. (In-stream), Pressure
Evaporator Inlet RH	Outlet Temp. (In-stream), Pressure
Evaporator Outlet Temp. (4 x 2 T/C)	ΔP of Evaporator.
Evaporator Outlet RH	Mass Flow Rate
ΔP of Evaporator	Temp. before/after the Compressor
ΔP of Nozzle (Air Velocity)	Temp. and Pressure before Exp. valve

The actual dimensions of the wind tunnel were chosen according to the size of the test heat exchanger (21 5/16" by 4"). While considering piping work and all other connections, the inside wind tunnel dimensions were fixed to 20" height and 25" width. The overall length was determined by ANSI/ASHRE 41.2-1987 Standard Methods for Laboratory Airflow Measurement and the space in the environmental chamber[11]. The total length of the open loop wind tunnel is 51". The final wind tunnel layout is shown in Figure 6.

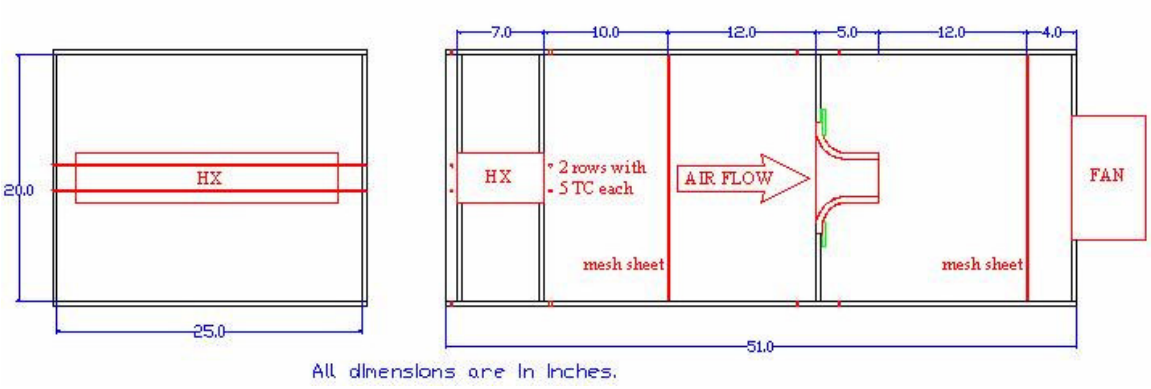

Figure 6: Wind Tunnel Layout

To make the duct accessible from all sides and to be able to visually monitor the conditions inside at any time, the side walls were made out of clear acrylic plastic sheet and all other sides were made out of polypropylene plastic sheets. Figure 9 shows the wind tunnel with its top opened, close to its complete construction.

All corners were held together with sheet metal angles and, during construction, silicone was used as the primary sealant. Additional aluminum duct tape was applied inside the duct as a secondary sealant.

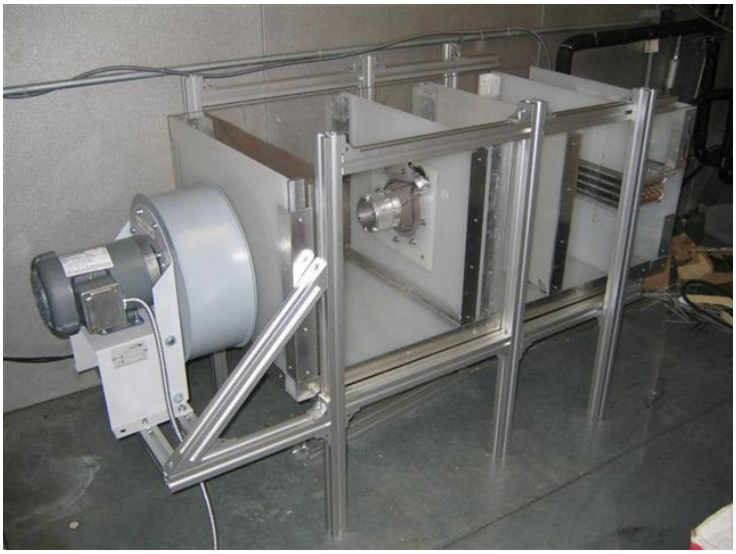

Figure 7: Picture of the Wind Tunnel

4.3.1 Wind Tunnel Fan

In order to determine a suitable fan motor for the wind tunnel, a pressure drop estimation was performed.

The wind tunnel pressure drop is calculated by summing up the pressure drops across the duct, heat exchanger, mesh sheets and nozzle.

The inner wind tunnel dimensions are 25" by 20" (0.64m by 0.51m). The area and perimeter could therefore be calculated. By using equation 1 [12], the hydraulic diameter was calculated.

$$D_h = \frac{4 \cdot area}{perimeter} = 0.564\,m \qquad \textbf{(1)}$$

The given maximum air flow rate is 240 cfm ($0.1133 m^3/s$). Therefore, the mean velocity of the air flow in the duct is 0.4 m/s. The kinematic viscosity, ν, at -17.8ºC according to air side test conditions is $1.197*10^{-5}$ m^2/s. Knowing ν, the Reynolds number can be determined by equation 2 [12].

$$\mathrm{Re} = \frac{D_h \cdot V}{\upsilon} = 16.55 \qquad \textbf{(2)}$$

The duct friction factor was also considered. By choosing the roughness factor from Table 1 in ASHRE fundamentals 2001 SI - 34.71[12], ε is equal to 0.03. The friction factor was calculated using equations 3 and 4 [12].

$$f' = 0.11 \cdot \sqrt{\frac{\varepsilon}{D_h} + \frac{68}{\mathrm{Re}}} = 0.157 \qquad \textbf{(3)}$$

If $f' \geq 0.018$ then $f = f'$ **(4)**

The length of the duct is 51" (1.29 m) and the density of air at -17.8ºC is about 1.365 kg/m^3. The pressure drop through the duct itself, therefore, can be calculated using equation 5 [12].

$$\Delta p = \frac{f \cdot l \cdot \rho \cdot V^2}{2 \cdot D_h} = 30.3\,Pa \qquad \textbf{(5)}$$

To determine the pressure drop across the heat exchanger, coil designer [13], a heat exchanger designing tool developed by CEEE, was used. A pressure drop of 75 Pa was calculated.

The nozzle pressure drop can be calculated with the air flow rate (AFR) according to test conditions up to 0.113 m^3/s and an assumed C_d value of 1. The real C_d value will be slightly smaller then 1, which is negligible for the pressure drop estimation. The nozzle throat diameter was 3" and therefore the nozzle throat area was 0.00456 m^2. By rearranging equation 6 and using equation 7 [14], the maximum pressure drop of 411.0 Pa was calculated with equation 8.

$$w = AFR \cdot \rho = C_d A_{nozzle\,throat} \sqrt{\frac{2\rho\Delta P}{1-\beta^4}} \qquad \textbf{(6)}$$

$$\beta = \frac{d_{nozzle}}{D_h} \qquad \textbf{(7)}$$

$$\Delta P = \frac{1}{2} \frac{AFR^2}{A^2_{nozzle\,throat} \cdot C_d^2} \rho\left(1-\beta^4\right) \qquad \textbf{(8)}$$

According to ANSI/ASHRE Standard 41.2-1987 the mesh sheets installed in the duct have to have an open area of 50-60% of the total area [11]. Two mesh sheets were installed. The pressure drop across each of them was estimated to be 85 Pa.

This estimation leads to a total pressure drop of 686.3 Pa. The detailed addition is shown in Table 5.

Table 5: Total Wind Tunnel Pressure Drop

Wind Tunnel	30.3 Pa
Evaporator	75.0 Pa
Nozzle	411.0 Pa
Mesh Sheet (2x)	170.0 Pa
Total	686.3 Pa

Since the result is based on estimation, the pressure drop is assumed to be around 700 Pa. Therefore a fan with a rating of at least 2.81" of water (700 Pa) at 240 cfm had to be used.

A 0.5 horse power centrifugal blower for low temperature applications with a variable frequency drive ready motor was selected from CFM Continental Fan and installed into the wind tunnel. The fan curve is shown in Figure 8. As can be seen in the Figure 8, the fan is slightly oversized to ensure that it will work for the required application. The air flow rate is adjusted by a frequency inverter drive.

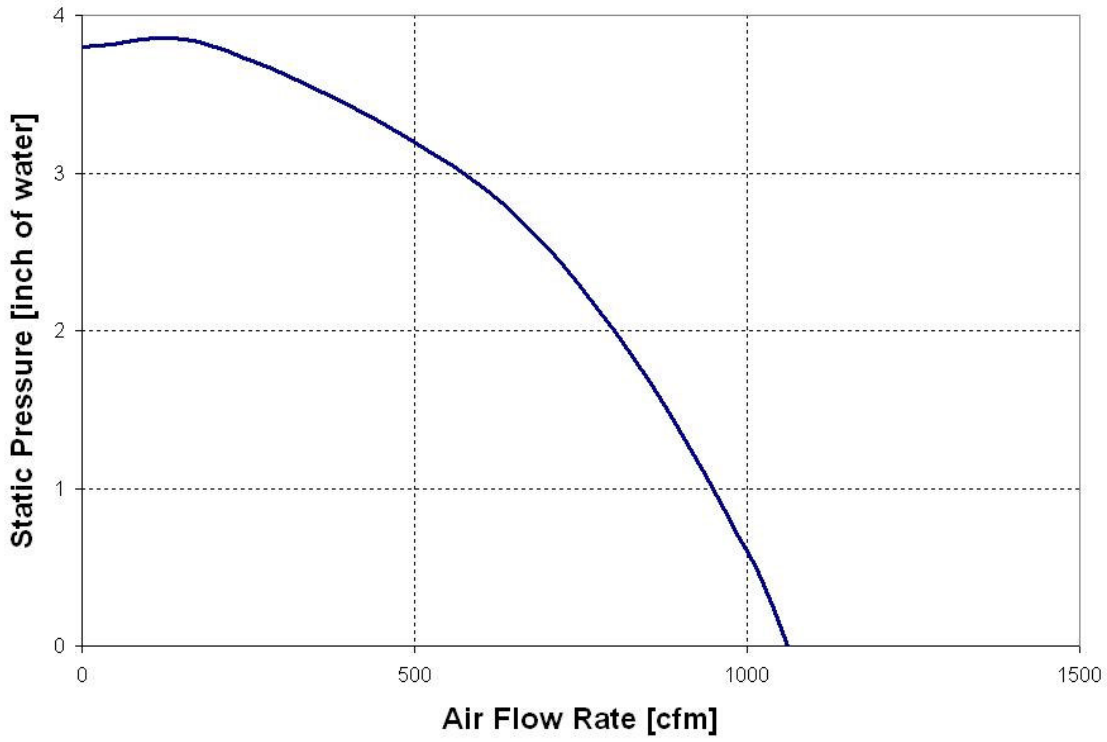

Figure 8: Fan Curve

4.3.2 Condensing Unit – Compressor Sizing

The condensing unit came with a compressor and a receiver. Both components were oversized for the current small capacity application. Consequently, the receiver was removed and the compressor needed to be replaced with a smaller capacity compressor. In order to choose the right size of compressor, an estimation of its capacity and displacement volume was performed.

Engineering Equation Solver (EES) was used to model the refrigeration cycle. Several assumptions were made in order to find the minimum required size of the compressor. Most of the cycle is fixed by the given test conditions.

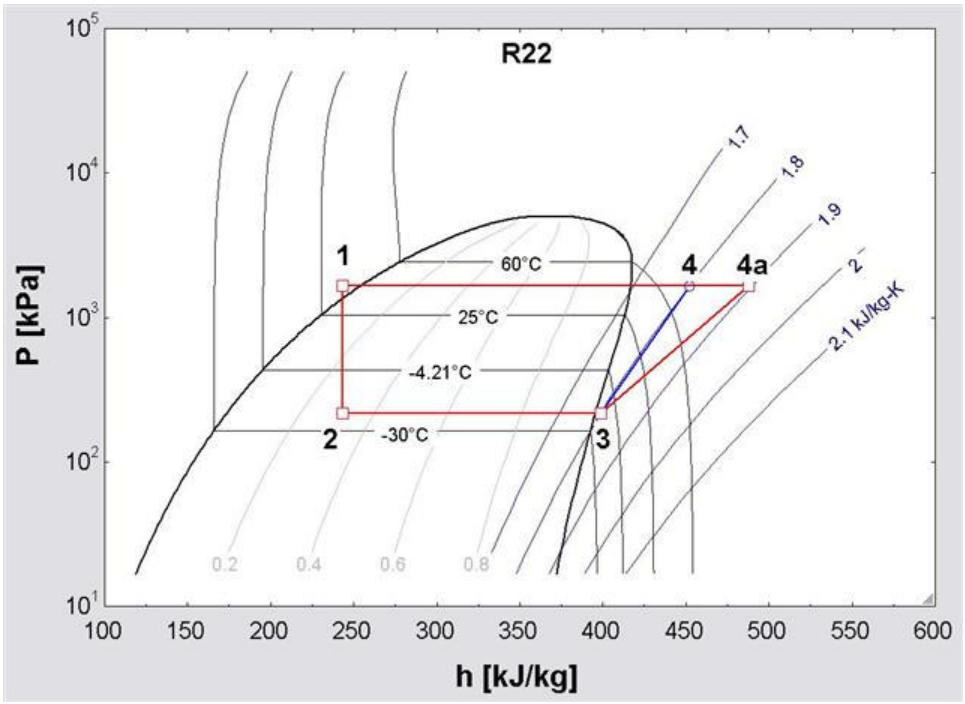

Figure 9: Real Test Cycle in P-h Diagram

Figure 9 shows the test cycle to estimate the compressor specifications. The first assumption is that the pressure stays constant on the high- and the low-side of the refrigeration cycle.

$$P_{low} = P_2 = P_{2a} = P_3;\ P_{high} = P_1 = P_4$$

The low pressure is defined by the evaporating temperature of -23.3°C and the high pressure is defined by the condensing temperature of 43.3°C, according to test conditions. The corresponding saturation pressures of R22 for P_{low} and P_{high} are 215.4 kPa and 1662.0 kPa, respectively.

The enthalpy of point one in Figure 9 is specified by temperature and high pressure. The temperature is also specified by 8.3°C sub-cooling, which corresponds to a temperature, t_1, of 35.0°C.

$$h_1 = f(P_{high}, t_1)$$

The expansion is assumed to be isenthalpic. Therefore h_1 is equal to h_2.

$$h_1 = h_2$$

The enthalpy of point three in the figure can be calculated with known temperature and low pressure. The temperature is specified by 4.5°C superheating, which corresponds to a temperature t_3 of -18.9°C.

$$h_3 = f(P_{low}, t_3)\ ;\ s_3 = f(P_{low}, t_3)$$

The capacity of the evaporator, Q_{evap}, is determined from the manufacturer's specifications and is equal to 0.5 kW. Therefore, it is possible to calculate the expected mass flow rate using the following equation:

$$\dot{m} = \frac{Q_{evap}}{(h_3 - h_2)} \qquad \textbf{(9)}$$

The expected mass flow rate is 3.22 g/s. An ideal compressor would have isenthalpic compression, corresponding to point 4 in Figure 9, but in reality, there is no ideal compressor. Using CEEE's past experience results for similar compressors the isentropic efficiency was assumed to be 0.6, the volumetric efficiency to be 0.7, the rotations per minute were assumed to be 3500 and the motor efficiency to be 0.85.

Given the assumed values, it is possible to calculate the displacement volume and the assumed compressor power using eqs. 10-12.

$$h_4 = f(P_{high}, s_3)$$

$$\eta_{isen} = \frac{h_4 - h_3}{h_{4a} - h_3} \qquad \textbf{(10)}$$

$$W_{comp} = \frac{\dot{m} \cdot (h_{4a} - h_3)}{\eta_{motor}} \qquad \textbf{(11)}$$

$$\eta_{vol} = \frac{\dot{m}}{\rho_3 \cdot V_{dis} \cdot RPM} \quad \textbf{(12)}$$

The displacement volume is assumed to be 8.44 cm^3 and the power consumption should be around 300 W. After an intensive search in the laboratory, a suitable compressor meeting the above criteria was found. It is a Samsung 44A080HU1EB with a displacement volume of 11.5 cm^3 and a nominal power consumption of 740 W. The nominal power consumption is higher than the estimated power consumption. This, however, does not matter since the heat exchanger is what is being evaluated, not the entire system. It is more important that the displacement volume is in the same target range. In order to be able to control the refrigeration cycle, a hot gas bypass was installed to adjust the refrigerant mass flow rate.

4.4 Instrumentation

As shown in Figure 5, a variety of sensors were installed in the system. This chapter specifies each sensor, including its range and error.

4.4.1 Pressure Transducers

Figure 10: Setra Pressure Transducer 280E

Four pressure transducers from Setra Systems, Inc. (model 280E) were installed at the following locations.

Table 6: Pressure Transducer - Locations and Specifications

Location:	**Specification:**
High pressure side:	
Compressor Outlet	0-500 psia
Expansion Valve Inlet	0-500 psia
Low pressure side:	
Evaporator Inlet	0-500 psia
Evaporator Outlet	0-500 psia

All pressure transducers were calibrated over their entire range. Additional calibration points were measured around the expected high and low test pressures. This procedure was done to increase local accuracy for the transducers at their operating range. The calibration showed that the pressure transducers have a 99.99% fit with the linear trend line in excel for all of them. The accuracy is ±0.11% full-scale accuracy

4.4.2 Differential Pressure Transducers

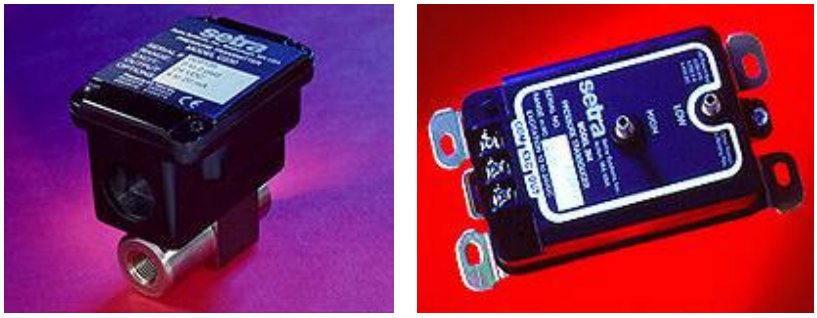

Figure 11: Differential Pressure Transducer

left: Setra 230; right: Setra 264

Three differential pressure transducers from Setra Systems, Inc. were installed for the measurement of the pressure drop, two of them on the air-side and one of them on the refrigerant-side. The range was chosen according to the calculations of the duct pressure drop.

Table 7: Differential Pressure Transducers – Locations and Specifications

Air-side:	**Range:**
Across heat exchanger: Setra 264	0-1" H_2O
Across nozzle: Setra 264	0-2.5" H_2O
Refrigerant-side:	
Across Hest Exchanger: Setra 230	0 - 25 psid

The differential pressure transducers factory calibration data were used. The accuracy of the Setra models 230 and 264 are ±0.25% and 264 ±1% full-scale accuracy, respectively.

4.4.3 Thermocouples

In order to control and understand the behavior of the cycle characteristics, many thermocouples were installed on refrigerant-side and air-side. Four in-stream thermocouples were installed on the refrigerant side and nine thermocouple grids were installed on the air-side. The different temperature measurement locations are listed below.

Table 8: Thermocouple Locations – Air-side

Air-side:	
Heat exchanger inlet	2 t/c grids horizontal
Heat exchanger outlet	4 t/c grids to divide the area into quarters
Nozzle outlet	1 t/c grid of six thermocouples

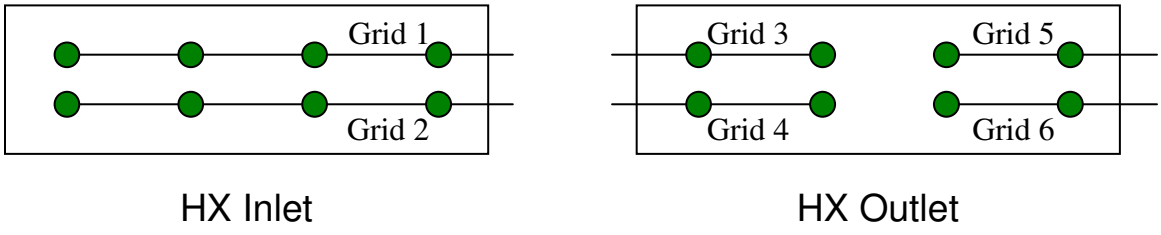

Figure 12: Test Heat Exchanger T/C Grid Location

Table 9: Thermocouple Locations – Refrigerant-side

Refrigerant side:	
High pressure side:	
Compressor Outlet	in stream thermocouple
Expansion valve Inlet	in stream thermocouple
Low pressure side:	
Evaporator Inlet	in stream thermocouple
Evaporator Outlet	in stream thermocouple
Compressor Inlet	surface thermocouple

All thermocouples used are T-type with an accuracy of ±0.5°C or less. Calibration was performed with an ice bath and boiling water. Additional two RTD thermocouples were installed in the middle of the HX inlet and the nozzle outlet because of their high accuracy of ±0.1°C or less. The RTD thermocouples are used to calculate the energy balance of the system.

4.4.4 Relative Humidity and Temperature Sensor

The humidity control plays an important role for frost formation study. Therefore, it is important to have an accurate measurement of the relative humidity. The test conditions require a humidity sensor which can operate in temperatures around 0°F (-17.8°C). Therefore, a Vaisala HMP 233 temperature and humidity sensor was used. The Vaisala HMP 233 has an operating range from 0 to 100% relative humidity and -40°C to 80°C. The accuracy for the humidity measurement in the applied range is ±1%.

The temperature sensor paired with the humidity sensor is a PT 100 RTD. It ranges from -40 to 80°C with an accuracy of ±1°C.

4.4.5 Mass Flow Meter

The refrigerant mass flow rate was measured with a Coriolis type mass flow meter. Specifically, the mass flow meter is a Micromotion Inc. model CMF025M, with a temperature range of -50°C to 125°C, a maximum pressure of 10 MPa, and an accuracy of ± 0.1% for the range of 0 to 5g/s of liquid fluid. It was installed at the condenser outlet where the refrigerant density is highest among the cycle state points.

The mass flow meter was purchased and factory calibrated for the range of 0 to 5g/s according to the cycle simulation.

4.4.6 Power Consumption Measurement

Power measurement for the refrigeration system is not a special interest since the heat exchanger performance is the major investigation. The power consumption of the electric defrost heater during the defrost cycle, however, is an important factor to record. A watt meter was connected to the electric defrost heater to measure the power consumption during its operation. The specifications of the wattmeter, GH-002D from Ohio Semitronics, Inc., are input 0-300 V, 0-5 A and an output of 0-10 VDC. The accuracy is ± 0.2 % of reading regardless of variations in voltage, current, power factor or load.

4.5 Nozzle

The nozzle was sized according to the test conditions of 210/240 cfm air volume flow rate. ANSI/ASHRE 41.2-1987 "Standard Methods for Laboratory Airflow Measurement"[11] sets the throat velocity of any nozzle from not less than 15m/s nor more than 35m/s for accurate measurement.

According to these requirements, a standard long-radius ASME nozzle with a throat radius of 3" was selected and used. A calibration was performed although the standard does not require a calibration for these types of nozzles.

4.5.1 Nozzle Calibration

The nozzle calibration is based on the Bernoulli Equation [15], shown below, and the conservation of mass.

$$P_1 + \frac{1}{2}\rho_1 v_1^2 + \rho_1 g h_1 = P_2 + \frac{1}{2}\rho_2 v_2^2 + \rho_2 g h_2 \qquad \textbf{(13)}$$

Since the wind tunnel has no height difference, h_1 equals h_2, and the change in density is negligible, so ρ_1 equals ρ_2. Then the equation simplifies to:

$$v_2^2 = v_1^2 + \frac{2(P_1 - P_2)}{\rho} \qquad \textbf{(14)}$$

Considering the air mass flow rate through the duct has to be the same as through the nozzle, the following equation is valid:

$$v_1 \rho_1 A = v_2 \rho_2 a \qquad \textbf{(15)}$$

Where A is the cross sectional area of the duct and a is the cross sectional area of the nozzle outlet.

By applying the same assumptions as above to this equation, it simplifies to:

$$v_1 = v_2 \frac{a}{A} \tag{16}$$

By combining equations 14 and 16, it is possible to calculate the velocity through the nozzle knowing the pressure drop across it.

$$v_2^2 = \frac{2(P_1 - P_2)}{\rho}\left(\frac{1}{1-(\frac{a}{A})^2}\right) \tag{17}$$

The air mass flow rate can be calculated by multiplying equation 13 with the local density and throat area of the nozzle as shown below:

$$\dot{m} = \rho \cdot a \cdot v_2 \tag{18}$$

The actual mass flow rate is smaller than the theoretical value. Therefore, a discharge coefficient value, C_d, is required to obtain the actual flow rate. The C_d value is formulated by "Fluid Meters and Their Applications" [16] based on flat plate boundary layer theory:

$$C_d = 0.9975 - 0.00653\left[\frac{10^6}{\mathrm{Re}}\right]^a \tag{19}$$

where Re is the Reynolds number and *a* is a Reynolds dependent factor.

For a Reynolds number smaller than 300,000, *a* equals 0.5 and for a Reynolds number larger than 3,000,000, *a* equals 0.2. If the Reynolds number is in between, linear interpolation applies. Knowing the theoretical velocity through the nozzle, the nozzle diameter and the kinematic viscosity, it is possible to calculate the Reynolds number and C_d value accordingly. The real mass flow rate can be calculated by the following equation [15]:

$$\dot{m} = C_d \cdot \rho \cdot a \cdot \sqrt{\frac{2(P_1 - P_2)}{\rho}\left(\frac{1}{1-(\frac{a}{A})^2}\right)} \qquad \textbf{(20)}$$

The calibration of the nozzle is used to verify that the theoretical value fits to the measured value. The calibration was done with an electric heater installed in front of the nozzle. By heating the air it is possible to measure a temperature difference which can be used to calculate how much the actual air flow rate is. Also the power consumption of the heater needs to be measured. The mass flow rate can be calculated by:

$$\dot{m} = \frac{P_{heater}}{c_p \cdot \Delta T} \qquad \textbf{(21)}$$

The result of a calibration is show in Figure 13. The calibration was within 2.2% of the theoretical value.

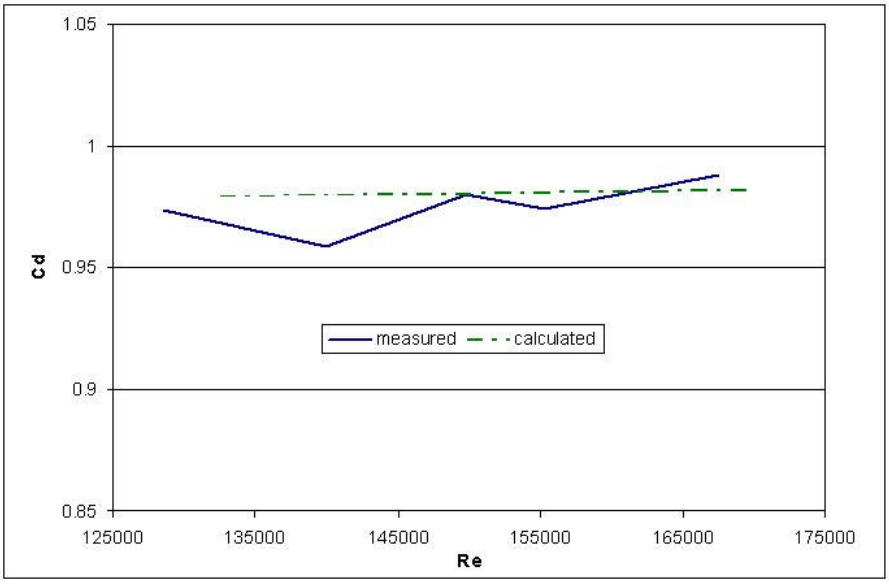

Figure 13: C_d versus Re - Nozzle Calibration

4.6 Defrost Control

The defrost control of the original evaporator, is specified by the manufacturer in a four step sequence operation.

Table 10: Cycle Sequence [17]

Step "A": Normal Refrigeration Cycle	Fan and Compressor on
	Defrost heater off
Step "B": Defrost Cycle	Defrost heater on
	Fan and Compressor off
Step "C": Coil Re-Cooling Cycle	Compressor on
	Defrost heater and Fan off
Step "D": Return to Normal refrigeration Cycle	Fan and Compressor on
	Defrost heater off

Initially the System is in the normal refrigeration mode like described in step "A".

At step "B" the defrost heater warms the coil to 55°F and the defrost termination thermostat opens, which de-energizes the defrost heater. This ends step "B" and begins step "C":

When the coil reaches a temperature of 35°F, the fan delay thermostat will close, ending step "C" and beginning step "D".

The unit is now back to operation as in step "A". This cycle will repeat two to four times a day in order to keep the capacity of the coil at an acceptable level according to the manufacturer.

The typical wiring diagram of the control is shown in Figure 14.

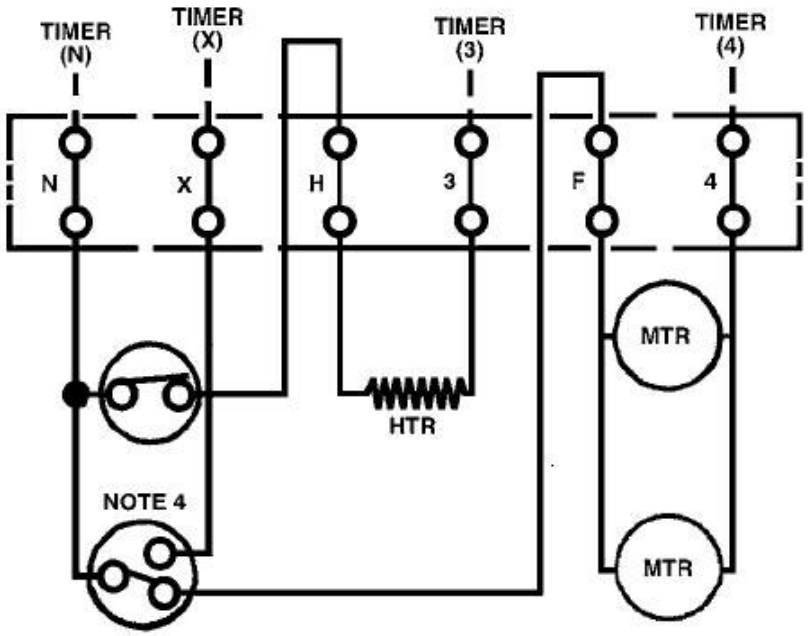

Figure 14: Typical Wiring Diagram for Thin Profile Electric Defrost Unit Cooler [17]

Since the heat exchanger should be tested under real operating conditions including cycling, it was necessary to establish a defrost control. To ensure that the control would be successful, a redundant system was created with 2 options: manual and fully automatic defrost control.

Manual control was done visually. Lights indicated if the heater was running and which line was energized. According to the lights the devices were turned on or off.

The automatic defrost control used either temperature or power and voltage measurements with a programmed algorithm to control the devices.

The electrical wiring diagram is shown in Figure 15. Three solid state relays control the defrost heater, wind tunnel fan and compressor. The activation can be done manually or by the data acquisition system (DAS), but it is important to ensure that they do not run together. Thermostat I is integrated into the system and turns off the heater.

The de-energizing of the heater determines Step "B" of the defrost cycle. If the defrost of the coil is not complete, it is possible to override thermostat I by closing the bypass switch. Thermostat II is used to determine the re-cooling of the coil. A control was set-up using lights to indicate which thermostat is turned on. The lights are used for a manual defrost. Voltmeters I and II are used to sense the voltage in each line to run a fully automatic defrost cycle.

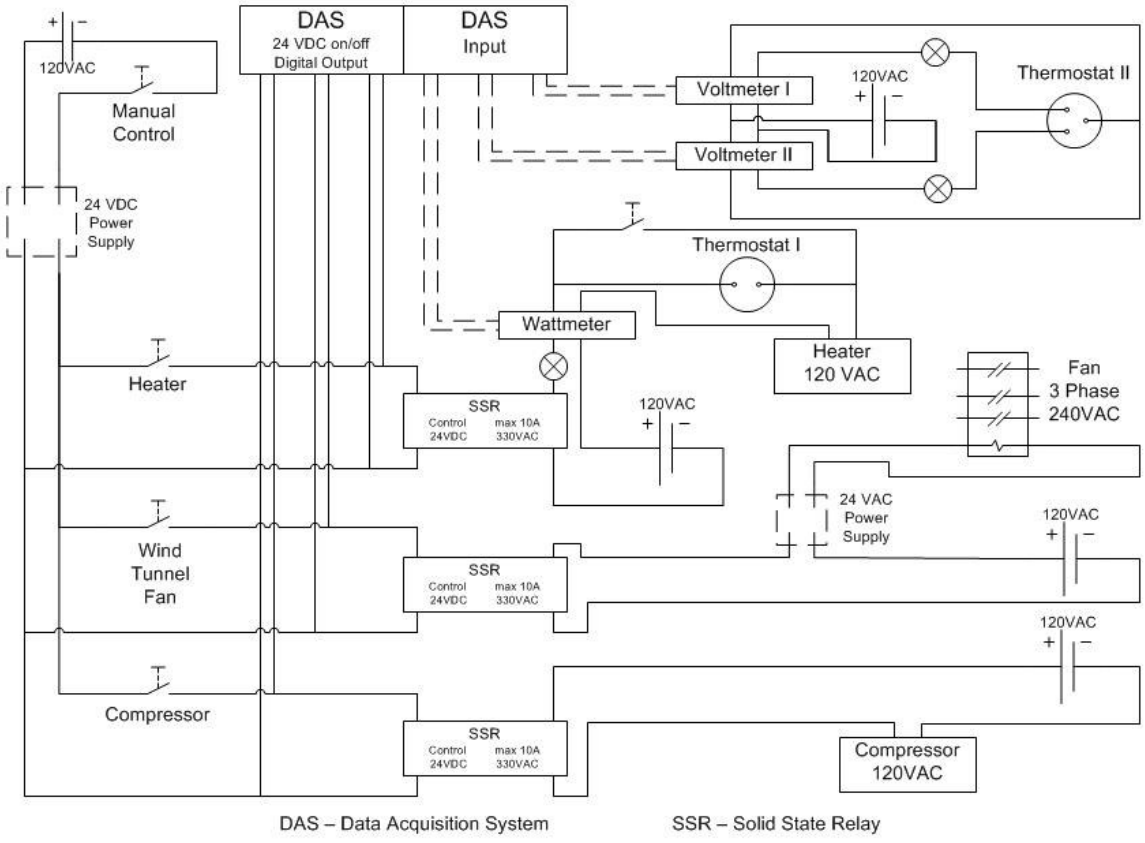

Figure 15: Electrical Wiring Diagram for Defrost Control

The fully automated cycle consists of four phases, exactly following the steps "A" through "D" as the manufacturer requires. Each stage has its own termination control. Step "A' is time determined. The time is a user input into the data acquisition system.

Step “B” is terminated by the reading of the wattmeter, once thermostat I opens the heater is de-energized and the wattmeter reading decreases to zero and the program goes to step “C”. Step “C” is terminated by thermostat II. The two voltmeters measure the voltage through the two wires entering thermostat II and, because only one wire is active at a time, the voltmeters sense when the switch occurs.

This is the end of the defrost cycle and the system enters the first loop and can be run continuously until the user aborts the program.

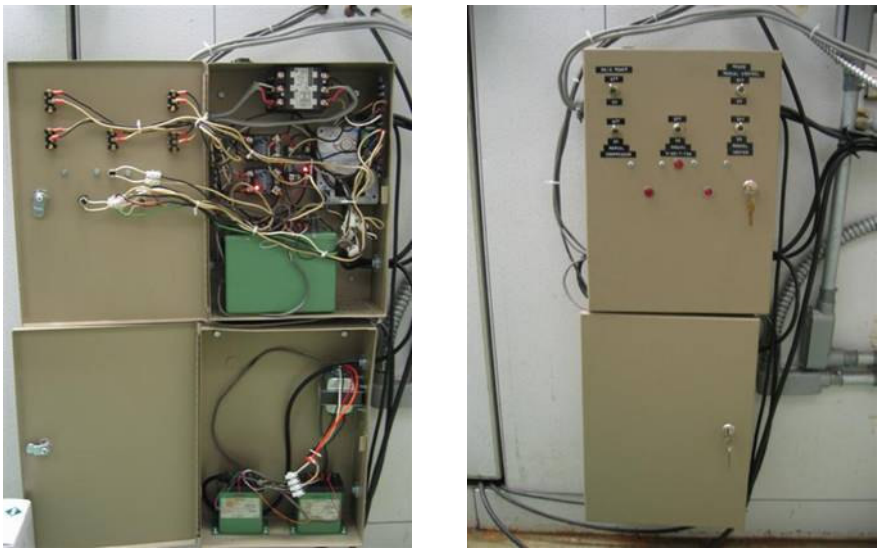

Figure 16: Picture of the Defrost Control Box

The cycle control is shown in Figure 16. Communication between all components is combined in the two boxes. The exact location of the defrost control switches is shown in Figure 17.

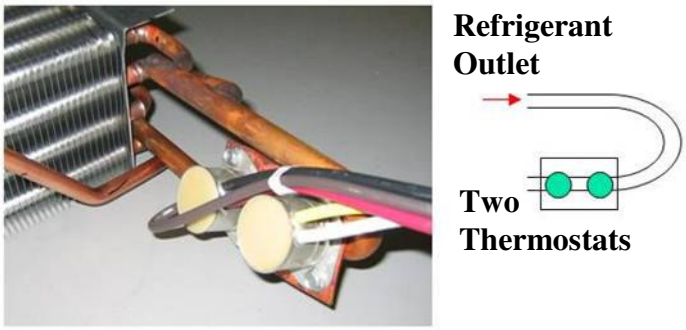

Figure 17: Defrost Control Setup

4.7 Data Acquisition System

All air- and refrigerant-side instruments were connected to National Instruments' FieldPoint data acquisition system (DAS) modules, which communicate with a LabView data acquisition software package. The FieldPoint DAS modules allow flexibility in instrumentation, as additional channels can easily be added or removed. These modules can be placed close to the individual parts of the experiment, which reduces the wiring length and other problems associated with long wiring.

A total of 31 channels were used to collect data (16 channels for the thermocouples and 15 channels for the analog inputs). The DAS was developed by using LabView to display the measured parameters (pressures, temperatures, mass flow rates and power consumption) in the form of numbers and graphs on the computer screen, as shown in Figure 18. Data was measured with a five second interval.

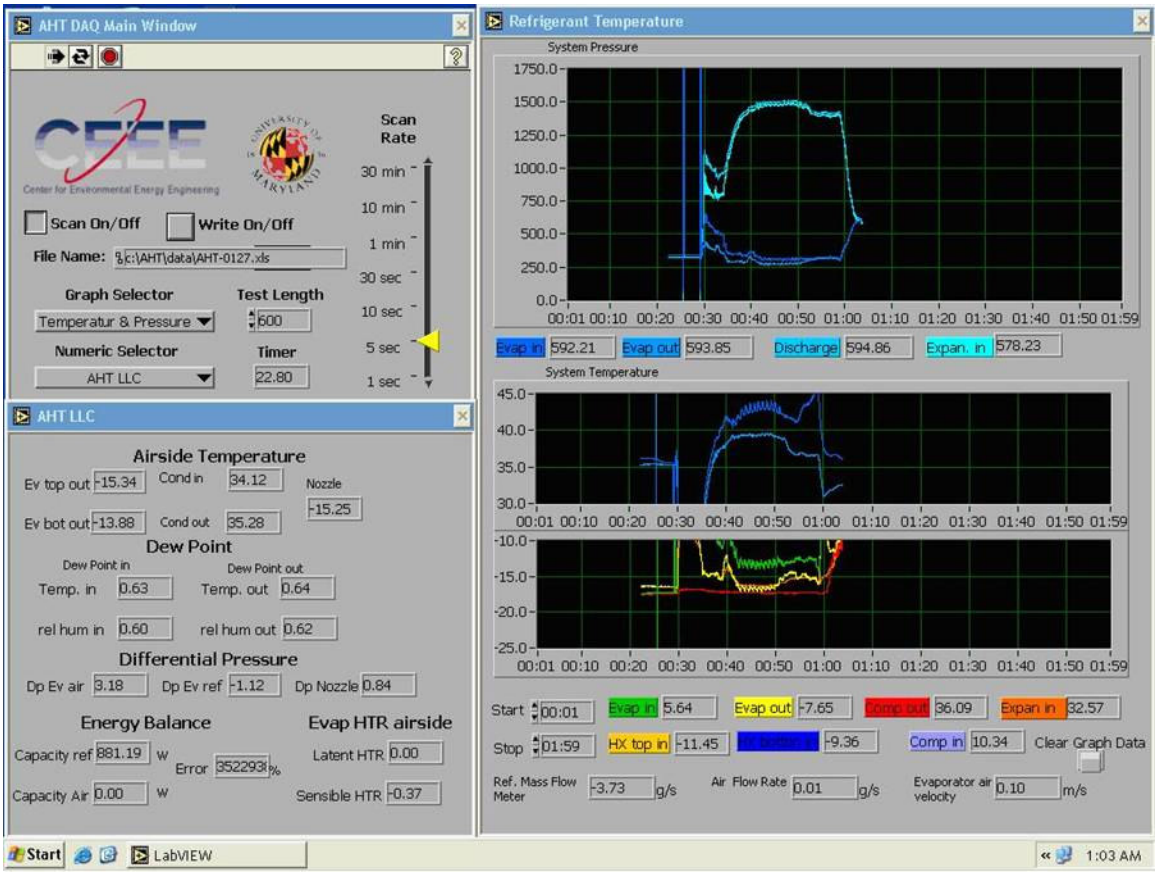

Figure 18: Screenshot of LabView Data Acquisition System

4.8 Test Procedure

In order to make a fair comparison between each test, an appropriate test procedure was developed. Since the test is a transient test, the energy balance fluctuates and conditions are never steady. Consequently, a pretest for the dry coil was added to the test procedure to show the validity of the test measurements and to adjust the settings to test conditions.

4.8.1 Pretest Procedure

A pretest is necessary to adjust the opening of the expansion valve and compressor bypass valve. Afterwards, no major adjustments are necessary during the actual test.

The pretest is conducted in a similar manner to the normal test but with some variations as follows:

- Test startup is the same except for the RH level
    1. Dehumidifier is on for the whole time
    2. Humidifier is off
- Test cycling is performed until step 7 except:
    1. Humidifier stays off
    2. Dehumidifier will be turned off, because it will cause additional load for the chamber and it could cause temperature fluctuations
    3. Step 7 will be the final step for this kind of test and the adjustment will be done in about 2 hours (60 min for compressor to reach steady state – 60 min adjustment afterwards)
    4. Pictures will be taken during the pretest to ensure that there is little or no frost on the coil

4.8.2 Test Procedure

This is the standard procedure for this test. Each test consists of three stages: startup, cycling and shut down. The exact chain of action is described below.

4.8.2.1 Startup

1. Check control of chambers and RH sensor position and function
2. Start decreasing the chamber temperature (humidifier off – dehumidifier on)
3. Turn on and adjust water supply for humidifier
4. Turn on wind tunnel fan (around 40 Hz)
5. Turn on DAS and computers
6. Check if all measured values are in the proper range
7. Turn on and check webcams and digital cameras (function and focus)
8. Arrange data-saving folders for new test
9. Check defrost control and provide heater power
10. When the cold chamber temperature reaches the -1°F control reading, turn off dehumidifier. Turn on humidifier and Set RH level

4.8.2.2 Cycling

1. Set cold chamber to 0°F
2. Make sure that all values are in the right range, especially inlet RH, HX inlet temperatures and the air volume flow rate through HX

   Start webcams and digital cameras to take pictures every 15 min
4. Start recording values of the DAS
5. Turn on condenser fan
6. Turn on compressor
7. Adjust values to test conditions (not more than 15 min)
8. Run for 6.5 hours from compressor start
9. Defrost cycle (automatic or manual):

a. Record movies with the webcam

b. Take pictures every minute

c. Start automatic or manual defrost cycle

d. After defrost

i. Save movie files

ii. Set webcams and digital cameras as in step 3

10. Run for another 6.5 hours

11. Defrost cycle (automatic or manual):

a. Record movies with the webcam

b. Take pictures every minute

c. Start automatic or manual defrost cycle

d. After defrost

i. Save movie files

ii. Set webcams and digital cameras as in step 3

12. Test complete. Turn off compressor and condenser fan

13. Turn off DAS recording

4.8.2.3 Shut down

1. Turn off webcams and digital cameras

2. Turn off heater power

3. Turn off humidifier

4. Increase cold chamber temperature incrementally to 45°F

5. Measure amount of collected defrost water after chamber is defrosted

Based on the above procedure, the total duration of one test can be estimated as follows:

Time estimation per test:

1. Preparation and Startup:	4h
2. 1st cycle:	6.5h
3. 1st defrost:	0.5h
4. 2nd cycle:	6.5h
5. 2nd defrost:	0.5h
6. Shut down:	1h
Complete test:	19.0h

5 Data Analysis

The analysis of the data was embedded into LabView. Modules based on XProps [18] were added to the LabView program so that it was possible to monitor the refrigeration and air capacities directly during testing. XProps is an enhancement to NIST's REFPROP7 database and provides additional integration capabilities.

5.1 Refrigeran-Side Performance

The analysis of the refrigerant-side performance requires the basic assumption of isenthalpic expansion in order to calculate the capacity of the coil. Therefore, the enthalpy at the evaporator inlet is assumed to be equal to the enthalpy at the expansion valve inlet. An in-stream thermocouple and an absolute pressure transducer were installed at the expansion valve inlet.

$$h_{evap\,in} = f(T_{\exp\,in}, P_{\exp\,in})$$

The enthalpy at the evaporator outlet could be measured directly as long as the refrigerant is superheated. Otherwise, a capacity calculation with the current setup is not possible.

$$h_{evap\,out} = f(T_{evap\,out}, P_{evap\,out})$$

The mass flow rate was measured with a coriolis type mass flow meter. Therefore, the capacity of the evaporator coil is calculated using the following equation:

$$Q_{evap} = \dot{m} \cdot (h_{evap\,out} - h_{evap\,in}) \qquad \textbf{(22)}$$

In order to calculate the degrees of superheating and subcooling, the saturation temperatures had to be determined.

$$T_{sat\ cond} = f(P_{Expan\ in})$$

$$T_{sat\ evap} = f(P_{Evap\ out})$$

Knowing the above temperatures, the degrees of superheating and subcooling could be calculated using the following two equations:

$$T_{\sup} = T_{evap\ out} - T_{sat\ evap} \quad \textbf{(23)}$$

$$T_{sub} = T_{sat\ cond} - T_{\exp\ in} \quad \textbf{(24)}$$

5.2 Air-Side Performance

The air side capacity is based on the measurement of five sensors: two RTD sensors, two relative humidity sensors and the differential pressure measurement across the nozzle. The temperature and relative humidity at these points were chosen because of their higher accuracy. The measurements of temperature and relative humidity are taken at the inlet of the test heat exchanger and at the outlet of the nozzle.

Implemented air property modules, based on XProps, used temperature, relative humidity and absolute pressure to calculate the enthalpies, humidity ratio and air density at the nozzle. The pressure at the inlet, $P_{hx\ in}$, is atmospheric pressure and was fixed for all calculations to be equal to 101.325 kPa. The pressure at the nozzle outlet, $P_{nozzle\ out}$, varies by the test due to the pressure drops through the heat exchanger, mesh sheet and nozzle. However, since the airside properties do not change significantly $P_{nozzle\ out}$ was fixed for all calculations to be to equals 101.0 kPa.

$$h_{hx\ in} = f(T_{hx\ in}, RH_{hx\ in}, P_{hx\ in})$$

$$h_{nozzle\ out} = f(T_{nozzle\ out}, RH_{nozzle\ out}, P_{nozzle\ out})$$

$$humRAT_{hx\,in} = f(T_{hx\,in}, RH_{hx\,in}, P_{hx\,in})$$

$$humRAT_{nozzle\,out} = f(T_{nozzle\,out}, RH_{nozzle\,out}, P_{nozzle\,out})$$

$$\rho_{nozzle\,out} = f(T_{nozzle\,out}, RH_{nozzle\,out}, P_{nozzle\,out})$$

The air side mass flow rate is calculated by equation 25. The equation was simplified by inserting all dimensions and other calibrated variables in order to have only two inputs: density and differential pressure..

$$\dot{m}_{air} = 0.974 \cdot \sqrt{4.160772 \cdot 10^{-5} \cdot \rho_{nozzle\,out} \cdot \Delta P} \quad \textbf{(25)}$$

The total capacity of the air side can be calculated with the following equation:

$$Q_{air\,side} = \dot{m}_{air} \cdot (h_{hx\,in} - h_{nozzle\,out}) \quad \textbf{(26)}$$

The total air side capacity is a summation of sensible and latent capacity. Since the current test is designed to determine frost formation, the latent capacity plays an important role. The sensible capacity can be calculated with the following two equations [19]:

$$c_p = 1805 \cdot \left(\frac{humRAT_{hx\,in} + humRAT_{nozzle\,out}}{2} \right) + 1.006 \quad \textbf{(27)}$$

$$Q_{sensible} = \dot{m}_{air} \cdot c_p \cdot (T_{hx\,in} - T_{nozzle\,out}) \quad \textbf{(28)}$$

The latent capacity can be calculated using the following equation:

$$Q_{latent} = \dot{m}_{air} \cdot (hunRAT_{hx\,in} - humRAT_{nozzle\,out}) \cdot latent\ heat \quad \textbf{(29)}$$

5.3 Energy Balance

In order to show the accuracy of the above measurements and calculations, an energy balance was conducted. The energy balance on the evaporator was calculated by

comparing the refrigerant-side capacity to the air-side capacity. The result is shown as the energy balance error in percent.

$$error = \left(1 - \frac{Q_{air\ side}}{Q_{evap}}\right) \cdot 100 \quad \textbf{(30)}$$

The average error during steady state for all tests was less than 5%.

5.4 Uncertainty Analysis

Systematic Error

The uncertainty of this experiment was determined using the Pythagorean summation of the discrete uncertainties as shown in Equation 41.

$$u_f = \sqrt{\left(u_{x_1} \cdot \frac{\partial f}{\partial x_1}\right)^2 + \left(u_{x_2} \cdot \frac{\partial f}{\partial x_2}\right)^2 + \cdots + \left(u_{x_n} \cdot \frac{\partial f}{\partial x_n}\right)^2} \quad \textbf{(31)}$$

Where

u_f is the overall uncertainty of function f resulting from individual uncertainties of $x_i...x_n$,

x_i are then nominal values of variables and

u_{x_i} are the discrete uncertainties

During the experiment several sources of error have been identified which are listed in the following table. The worst case temperature, pressure and mass flow rate was chosen.

Table 11: Uncertainty Analysis - Refrigerant Side Systematic Error

Measurement	**Accuracy**
Temperature	± 0.5°C or 2.6%
Pressure	± 3.8kPa or 1.7%
Mass Flow Rate	± 0.3%
Capacity	±0.6%

The uncertainty was calculated using Engineering Equation Solver (EES).

Random Error

The data used to calculate the random error is the pretest data, because it is at steady state. The average values and standard deviations were calculated with excel over a time period of 45 min. The chosen values to determine the random error are the highest throughout the 45 min time interval.

Table 12: Uncertainty Analysis - Refrigerant Side Random Error

	Average value	Std. Deviation	Error in %
Temperature	-23.9°C	0.25°C	1.0%
Pressure	1667.9 kPa	2.0 kPa	0.1%
Mass Flow Rate	2.426 g/s	0.006g/s	0.25%
Capacity	377.1 W	1.0W	0.2%

Total Error

The total error is the summation of the systematic and random error.

Table 13: Uncertainty Analysis - Refrigerant Side Total Error

	Temperature	Pressure	Mass Flow Rate	Capacity
Systematic Error	2.6%	1.7%	0.3%	0.6%
Random Error	1.0%	0.1%	0.25%	0.2%
Total Error	3.6%	2.8%	0.55%	1.2%

6 Test Results

The results of the heat exchanger tests are presented below. For each test the test conditions are fixed as described earlier. Only the air flow rate was varied from 210 cfm to 240 cfm. All measured data is shown for each test.

The test at 210 cfm was conducted for 5 cycles, at 240 cfm for 2 cycles, respectively. For all tests a pretest was conducted to adjust the system to the desired test conditions.

6.1 Fin-and-Tube Type Heat Exchanger – 210 cfm

This test was conducted with the specified test conditions with an air flow rate of 210 cfm. It was conducted for five frosting and defrosting cycles. The following figure shows the refrigerant side temperatures.

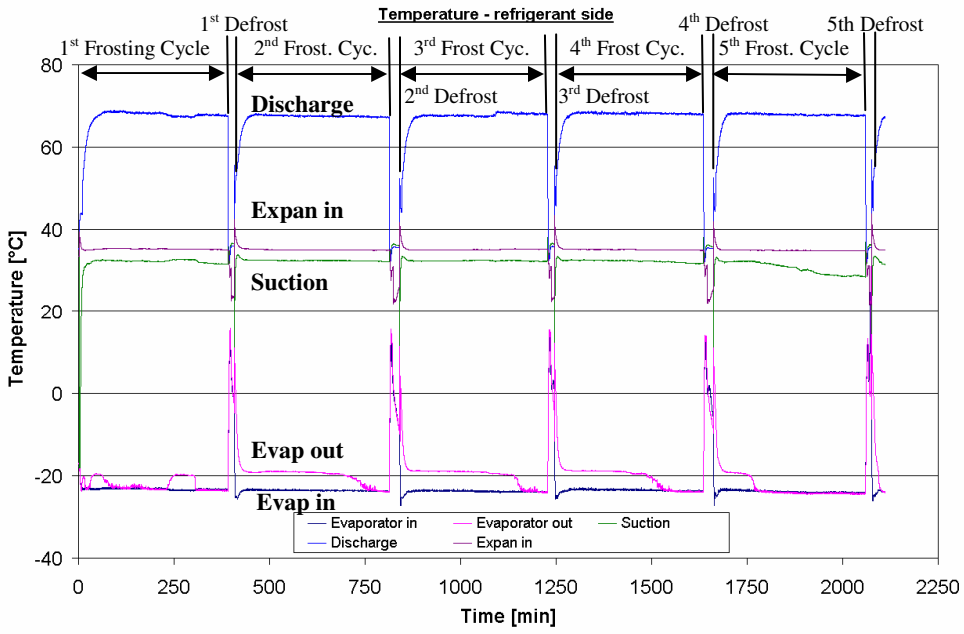

Figure 19: Refrigerant –Side Temperature versus Time at 210 cfm

A special focus is set on three temperatures: evaporator inlet, evaporator outlet and expansion valve inlet. The expansion valve inlet temperature has to be stable in order to provide constant inlet conditions into the evaporator coil. The difference in evaporator inlet and outlet is the superheat.

As described earlier the coil inlet and outlet has all together six thermocouple grids. The next figure shows them over time.

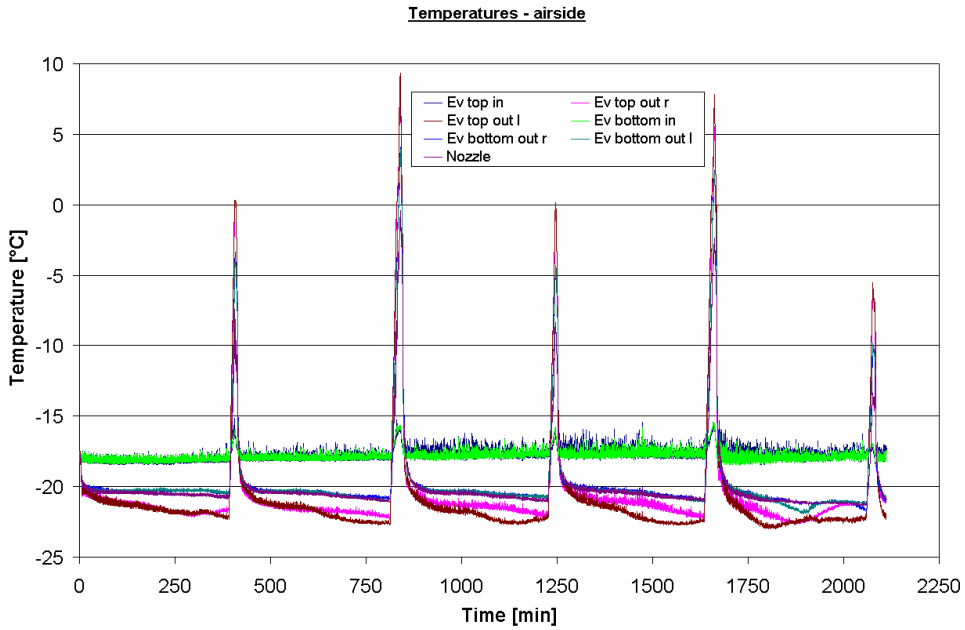

Figure 20: Evaporator Air-Side Temperature versus Time at 210 cfm

The difference in temperatures at the outlet of the coil is to explain with the frost buildup which starts growing from the bottom to the top of the coil according to the circuitry.

The condensing unit was placed into an environmental chamber. Since the system is very small in capacity and the receiver had been removed it was very sensitive to temperature fluctuations. Especially the condenser inlet temperature should ideally be

a straight line. The next figure shows the air side temperatures at the condenser inlet and outlet.

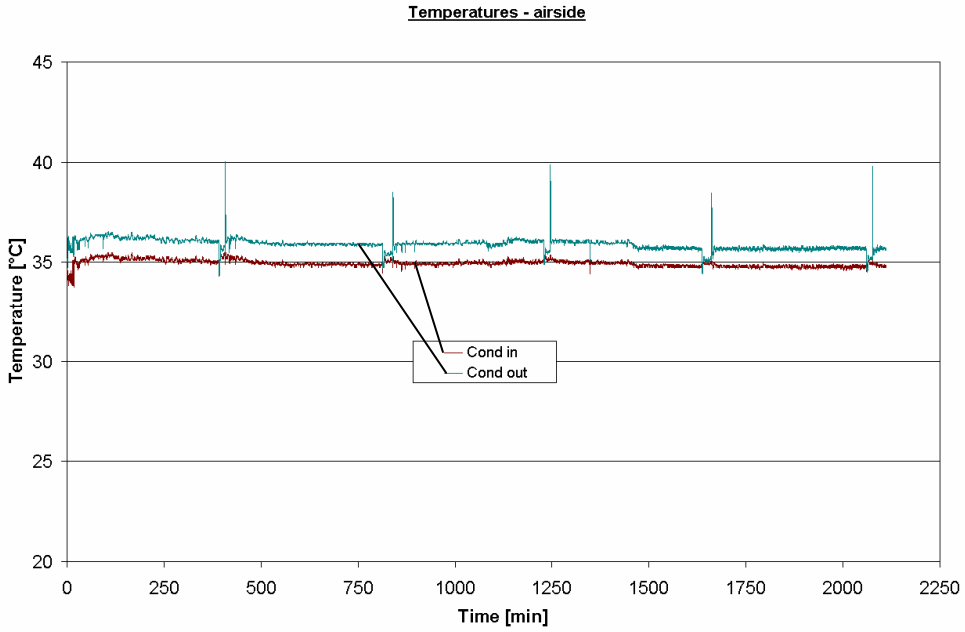

Figure 21: Condenser Air-Side Temperature versus Time at 210 cfm

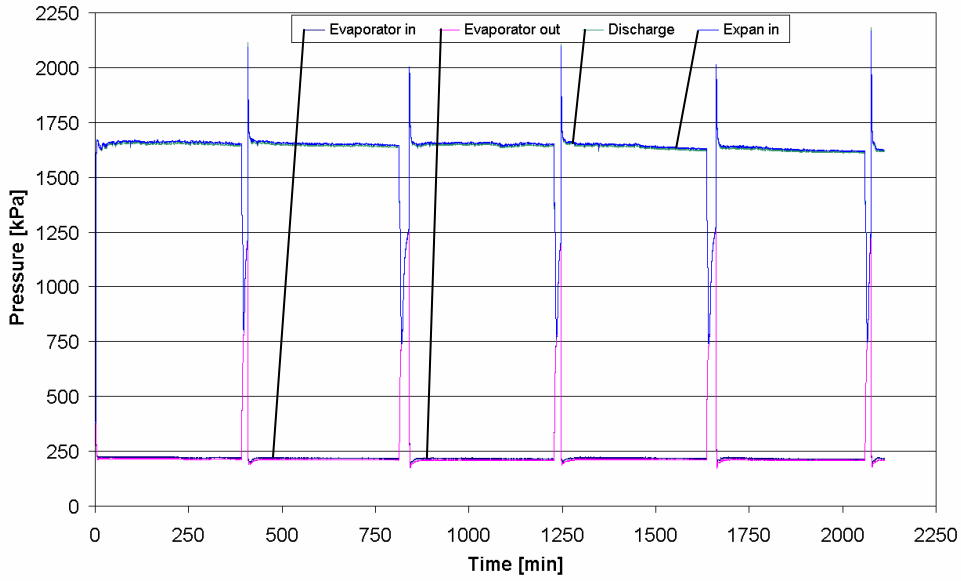

Figure 22: Pressure versus Time at 210 cfm

The system pressures are shown in Figure 22. The system pressure is used to adjust the condensing and evaporating temperatures. Therefore it was necessary to adjust it carefully. The pressure decrease towards the end of each cycle is to explain with superheat loss and therefore the whole system pressures shifted down.

The air and refrigerant mass flow rate is shown in Figure 23. The refrigerant side mass flow rate stays nearly constant, while the air side mass flow rate constantly decreases as frost builds up.

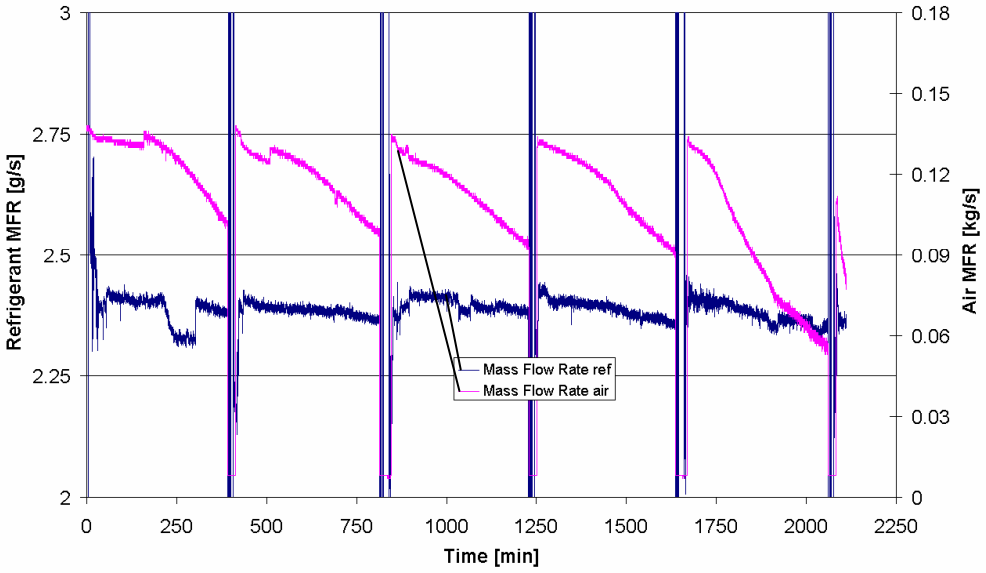

Figure 23: Mass Flow Rates versus Time at 210 cfm

The humidity level is an important measurement in this test. It was about the same for the first three cycles and then it was increased in order to see how much its effect on the coil is. The relative humidity for the inlet and outlet of the coil is shown in Figure 24.

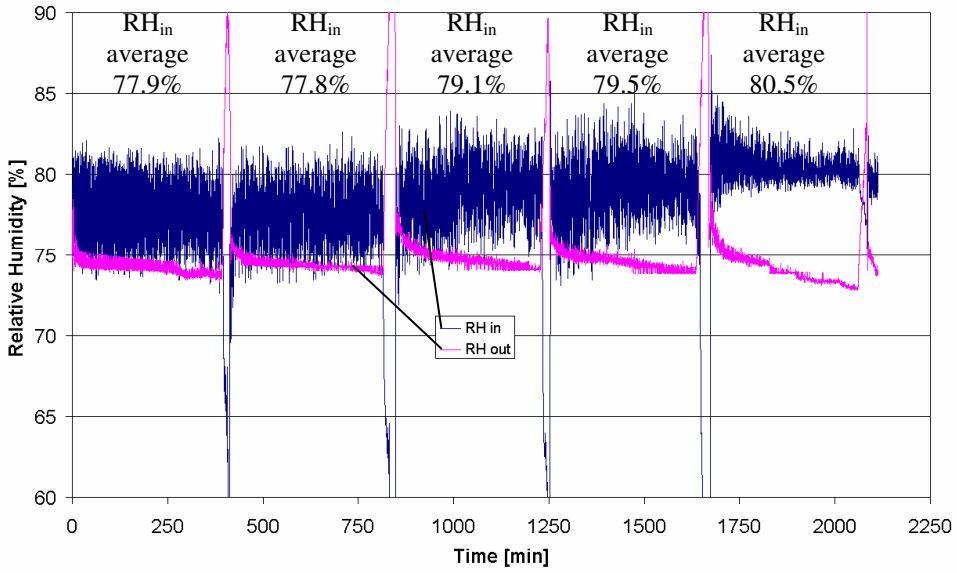

Figure 24: Relative Humidity versus Time at 210 cfm

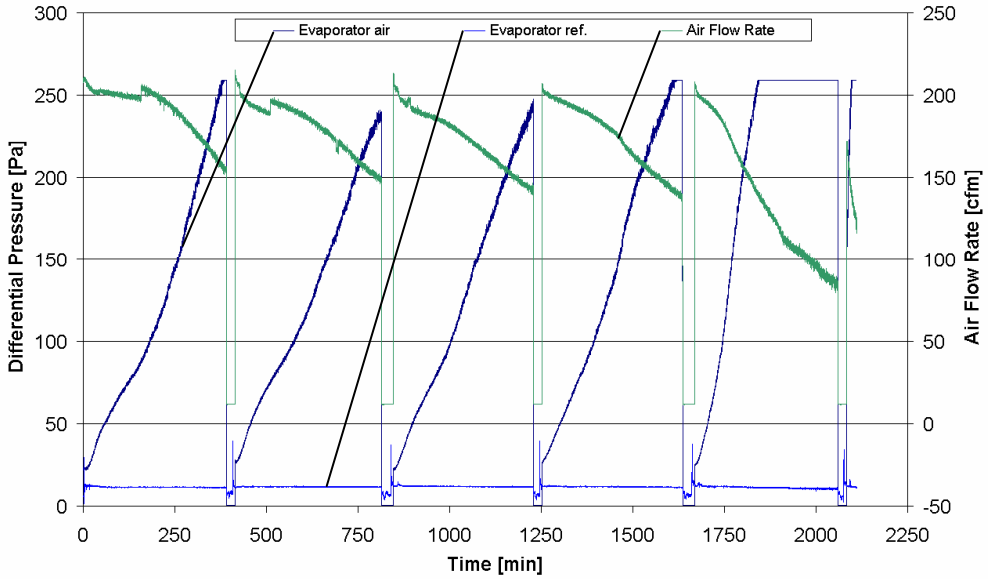

Figure 25: Differential Pressure and Air Flow Rate versus Time at 210 cfm

Figure 25 shows the air side and refrigerant side differential pressure of the coil and air flow rate. The refrigerant side differential pressure is constant though all cycles.

The air side differential pressure is increasing as frost builds up and the air flow rate is decreasing.

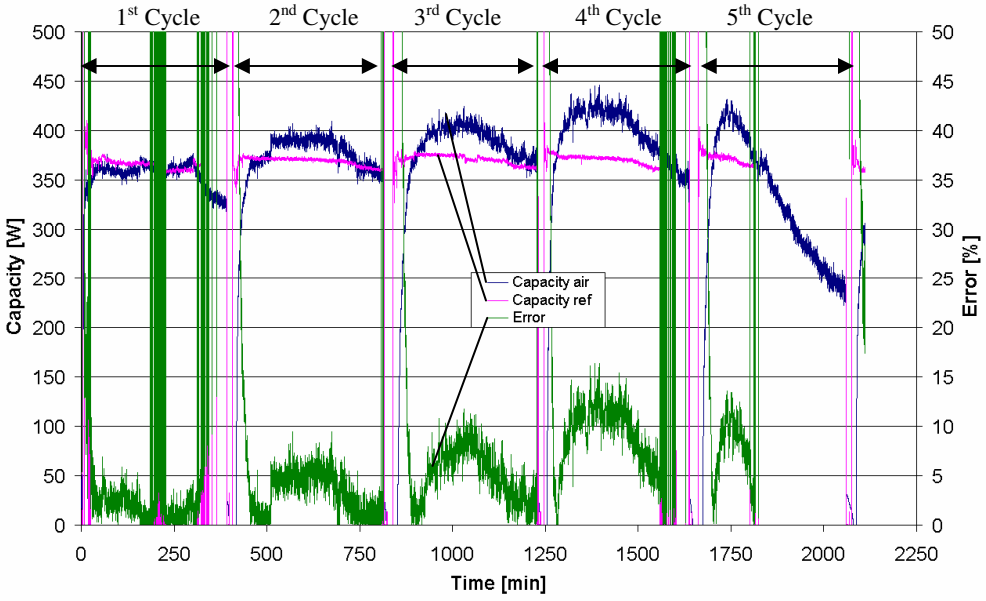

Figure 26: Capacity & Error versus Time at 210 cfm

The air side and refrigerant side capacities as well as their error are shown in Figure 26. The refrigerant side capacity can only be calculated when the outlet of the coil is superheated and vapor condition. That explains why it is not possible to show the refrigerant side capacity throughout each cycle. The error is not computable when there is no superheat. For the first cycle the capacities fit together very well and the error is below 5%. Throughout the other cycles the error increases, which can be explained with frost buildup at the sensor itself. The frost buildup will decrease the accuracy and slow down the response time of the sensor.

The superheat is the indicator if the coil is still able to evaporate all refrigerant. If frost builds up and blocks the air flow the heat transfer of the air side decreases and therefore the heat exchanger loses superheat. The following figure shows degrees of

superheating and sub cooling versus time. Sub cooling needs to be constant to provide constant inlet conditions into the evaporator coil.

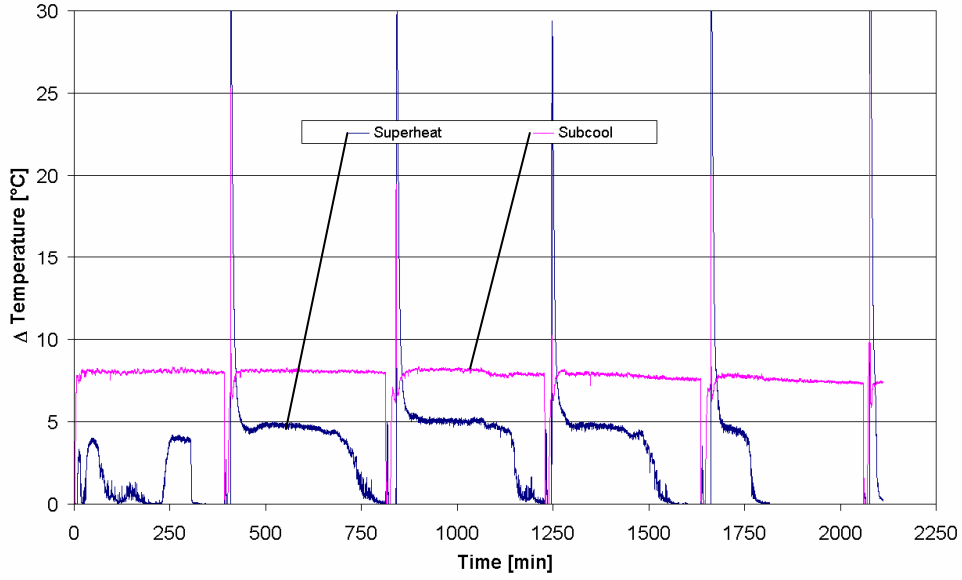

Figure 27: Degrees of Superheating and Subcooling versus Time at 210 cfm

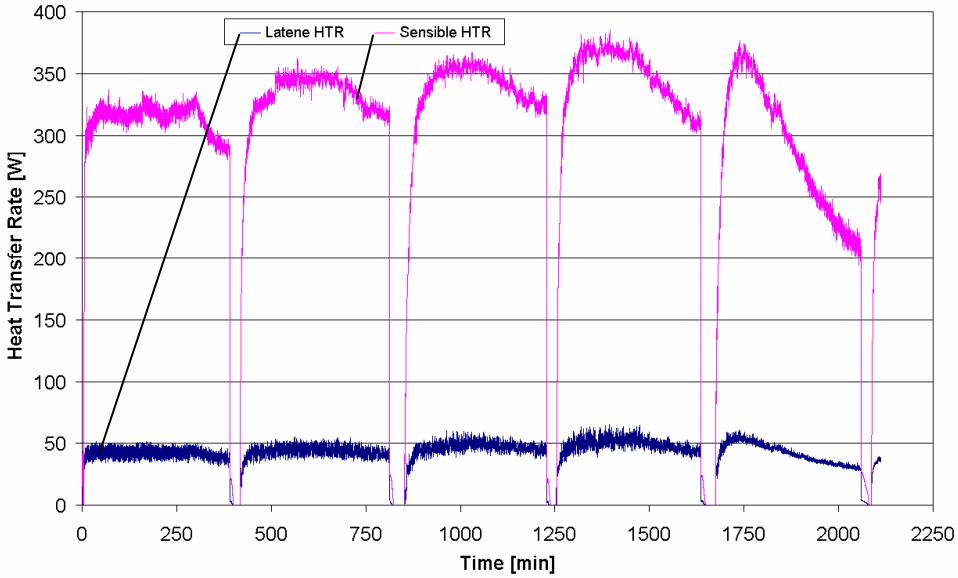

Figure 28: Latent and Sensible Heat Transfer Rate versus Time at 210 cfm

Figure 28 shows the calculated sensible and latent capacities. Obviously the latent load is pretty much constant, even with increased relative humidity, especially for the 5th cycle.

The defrost cycle behavior, heating time and re cooling time is shown in Figure 29. When the heater power consumption starts up is the end of the freezing cycle and the beginning of the defrost cycle. The temp control 2 regulates the refreezing period for the coil. And when it ends the defrost ends too and a next freezing cycle starts up.

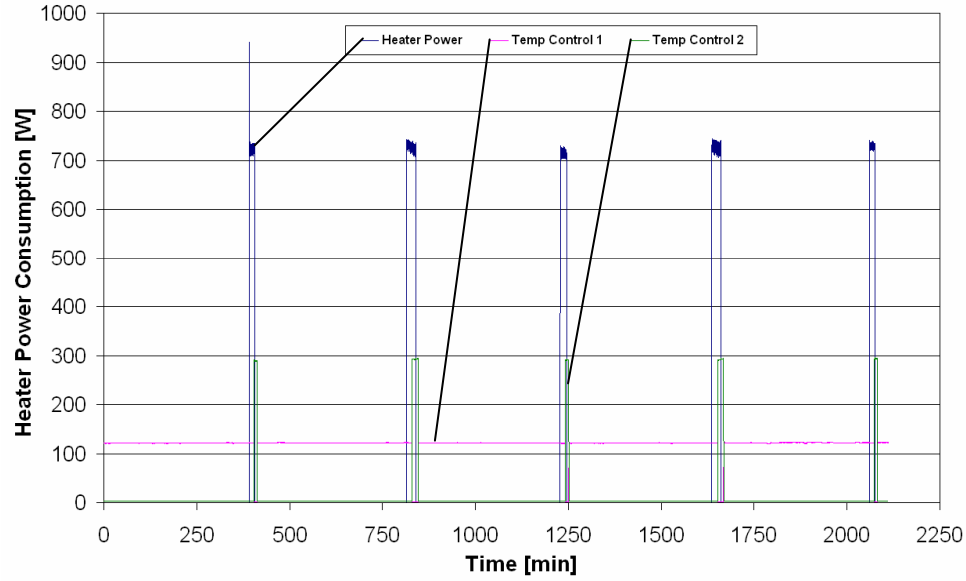

Figure 29: Defrost Heater Power versus Time at 210 cfm

The following Figures 30 to 39 show pictures taken at the inlet of the coil. All five freezing and defrosting cycles are shown in detail. Especially focus should be set for the startup picture of each freezing cycle, since the coil never drains completely and water refreezes.

Figure 30 shows the 1st frosting cycle. The pictures are in time steps of one hour in general and half an hour for the last picture. At the test start the coil is absolute dry.

Individual crystals are visible after 1 hour, which are the start of the frost formation. These single crystals start growing until the most of the surface is covered (picture at 2h). From there the crystals start to grow into the air passage (picture at 3h) and finally connect with each other blocking the air passage (picture at 4h). Even it seems like the air passage is blocked after 4 hours, the density of the frost is not high enough to totally block the air passage. During the following 2.5 hours frost densification happens. An interesting observation is that where the fins were bended and closer together the frost grew faster and heavily blocked the air passage.

Figure 31 shows the first defrost cycle. The defrost cycle time is not specified since two thermostats control the heater time and the re-cooling time of the coil. The first picture is essentially the same as at the end of the first frosting cycle for consistency, but it is the startup of the electric defrost heater of the evaporator. The second picture shows the coil at the time when the thermostat de-energized the electric defrost heater and the re-cooling of the evaporator coil begins. It is obvious that coil drainage is an important issue since many droplets of water stayed on the surface even after the defrost cycle. As shown in the third picture, which is taken at the end of the re-cooling sequence when the evaporator coil starts its normal freezing cycle. Here a lot of initial ice has formed on the evaporator coil.

Figure 32 shows the 2nd frosting cycle. The initial ice on the evaporator changes the frost formation tremendously. The ice crystals grow faster and also the interconnections in between two surfaces happen earlier. All over the evaporator coil is much more affected by frost. The measurement of the air volume flow rate supports this observation, as can be seen in Figure 25. At each freezing cycle startup it is in the same

range, but with the increase of the total frosting cycles the less air volume flow rate passes the coil at each end of the cycle.

The frost build up of the fourth cycle, shown in Figure 36, is very heavy, so that the defrost cycle, shown in Figure 37, is not able to remove all the ice from the inlet of the evaporator coil. Therefore the blockage of the coil occurs much faster and the fifth freezing cycle is not valid for a comparison with the others. Also the relative humidity level was changed for the fifth cycle to see how much the capacity gets affected. With an increase of the relative humidity the evaporator coil blocks quickly and build up a layer of ice right in front of it, as shown in Figure 38. The defrost cycle can not handle the huge amount of ice at the inlet of the coil, as shown in Figure 39.

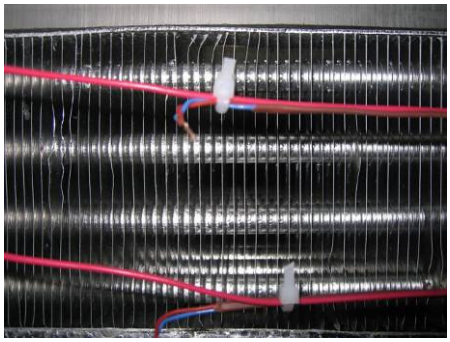

Startup

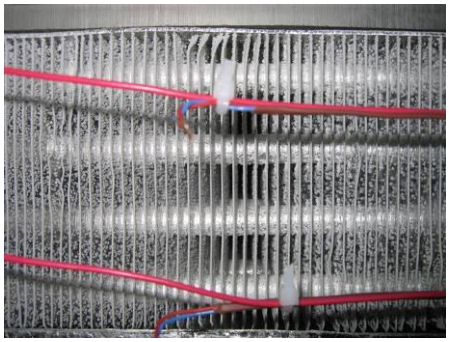

1h

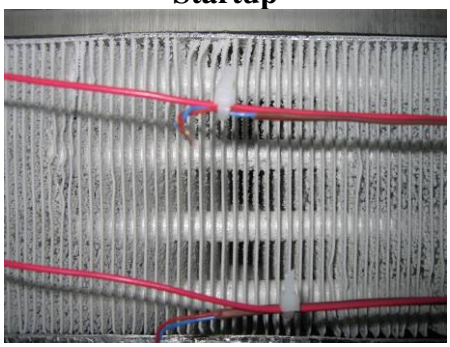

2h

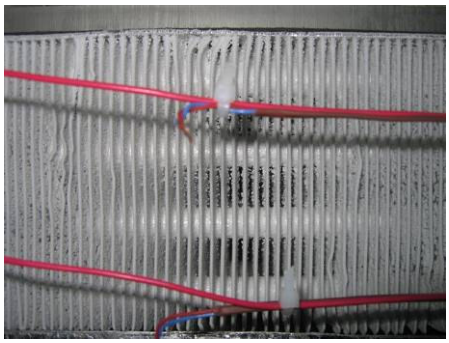

3h

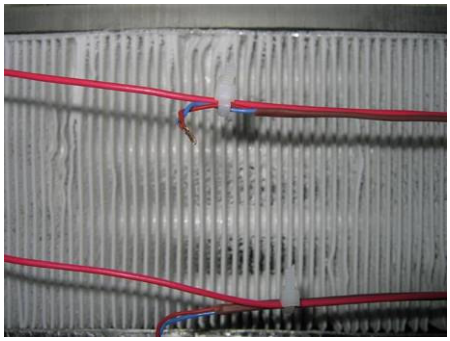

4h

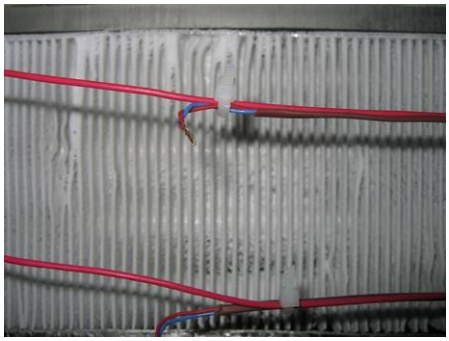

5h

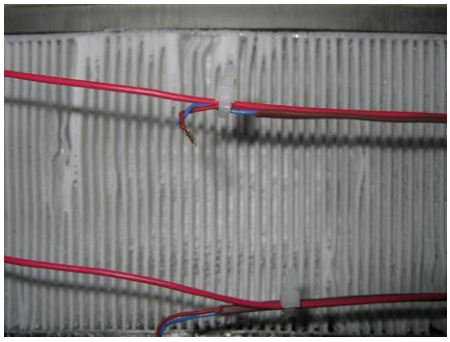

6h

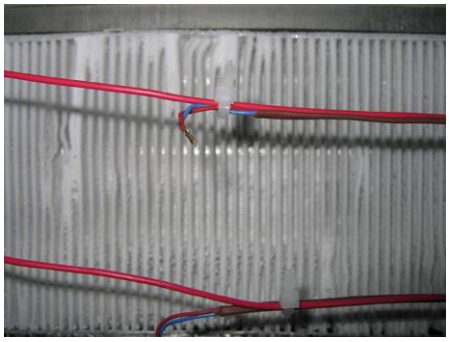

6.5h

Figure 30: 1st Frost Cycle – 210 cfm

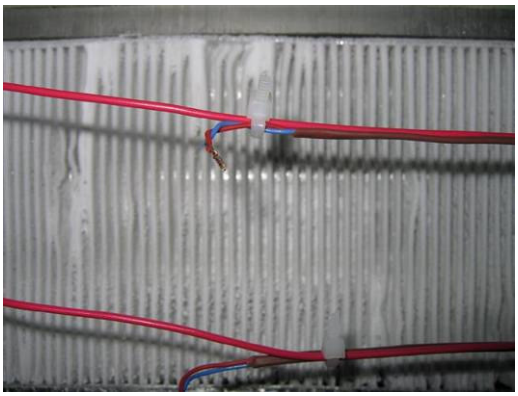

Start Defrost

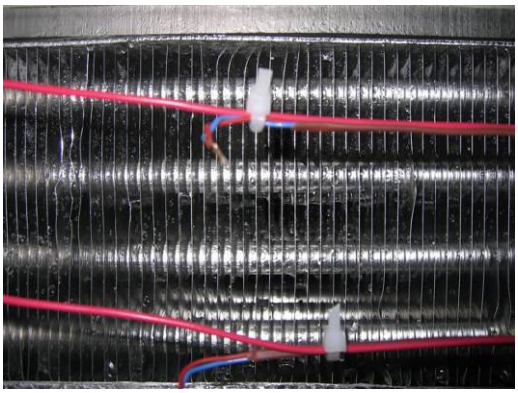

Heater Off – Compressor On

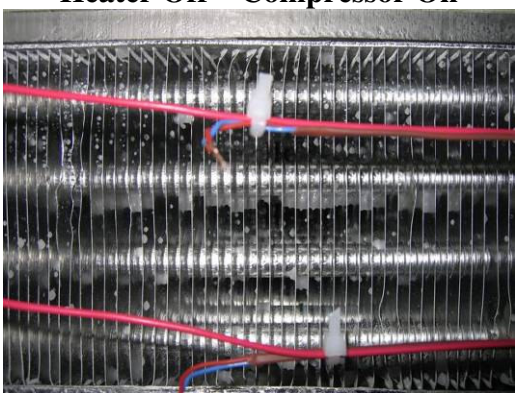

Fan On

Figure 31: 1st Defrost Cycle – 210 cfm

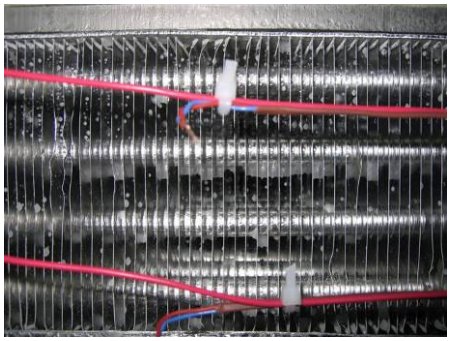

Startup

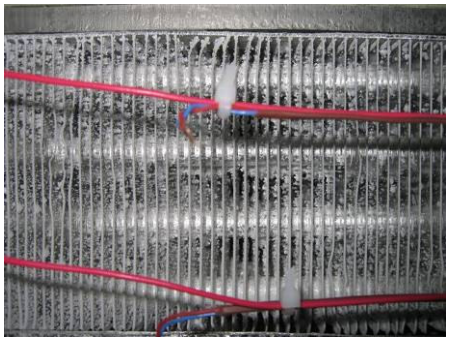

1h

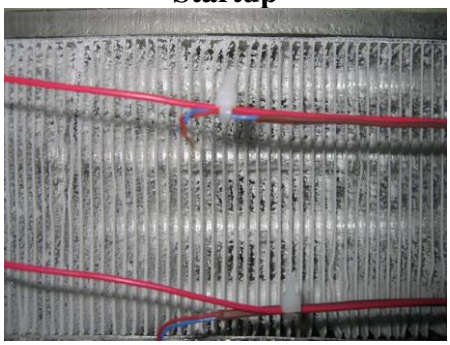

2h

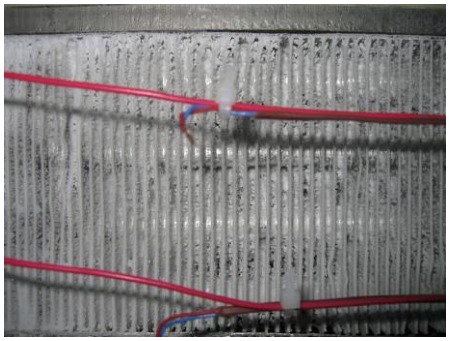

3h

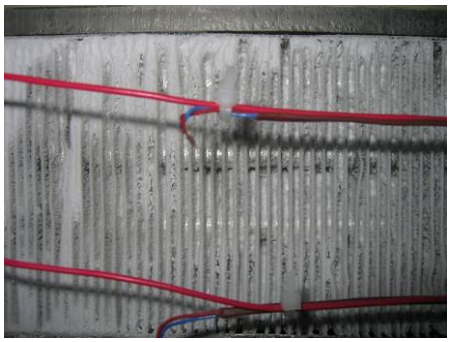

4h

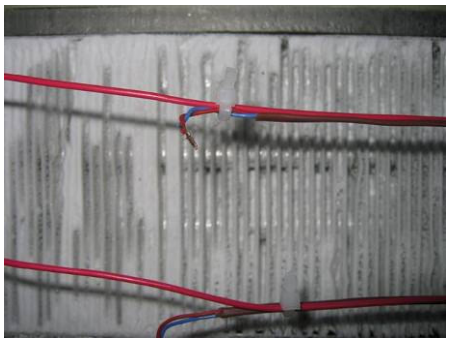

5h

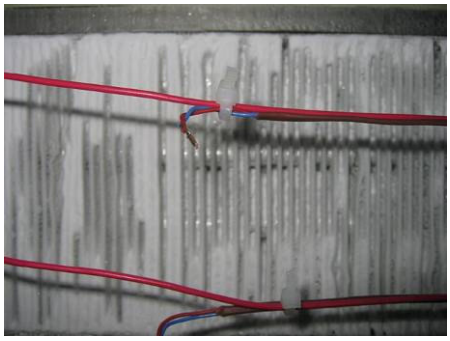

6h

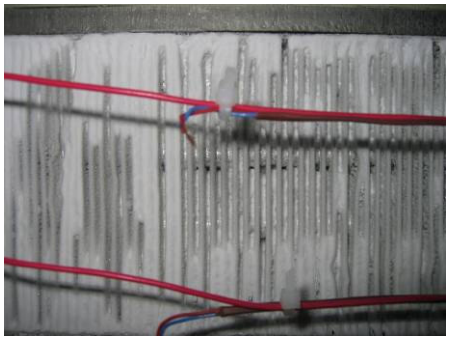

6.5h

Figure 32: 2nd Frost Cycle – 210 cfm

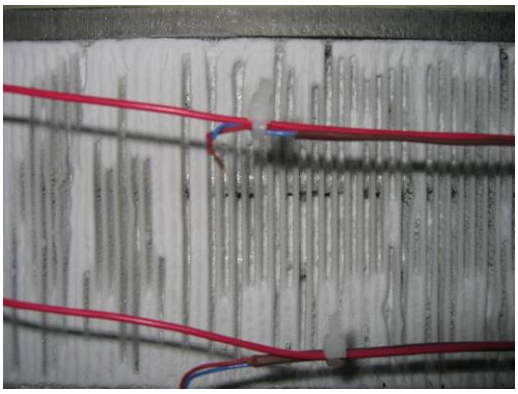

Start Defrost

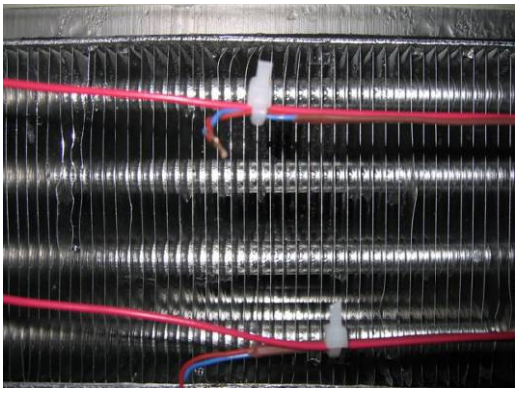

Heater Off – Compressor On

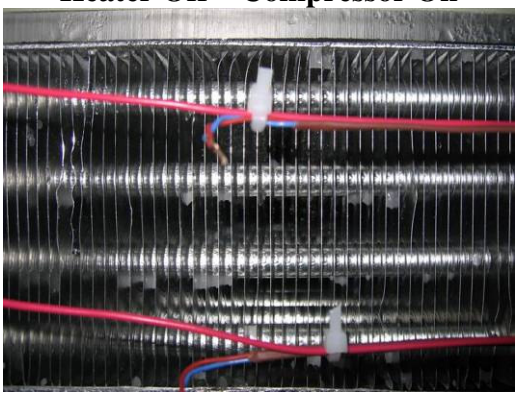

Fan On

Figure 33: 2nd Defrost Cycle – 210 cfm

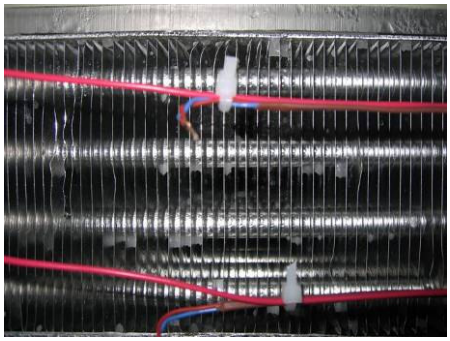

Startup

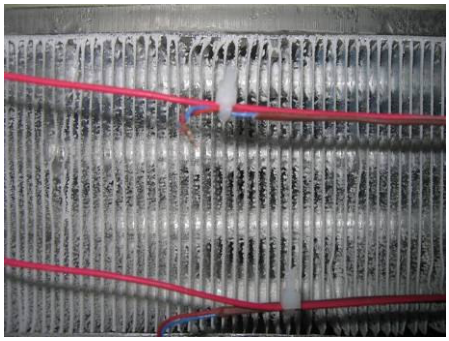

1h

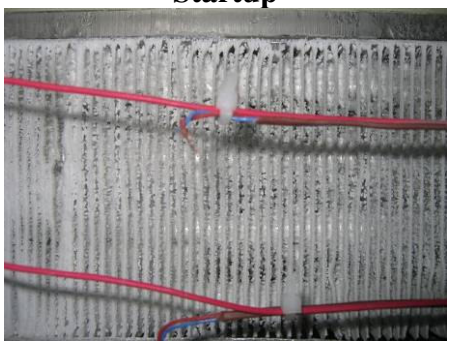

2h

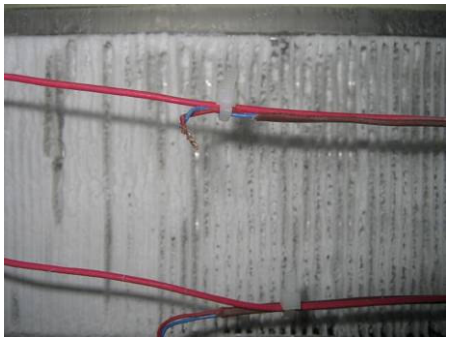

3h

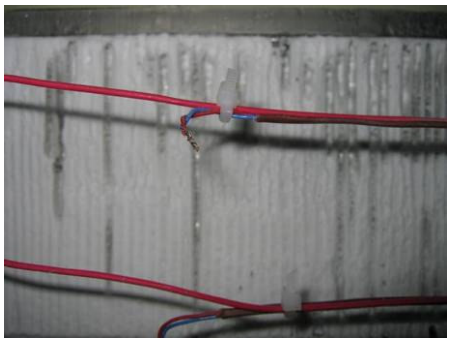

4h

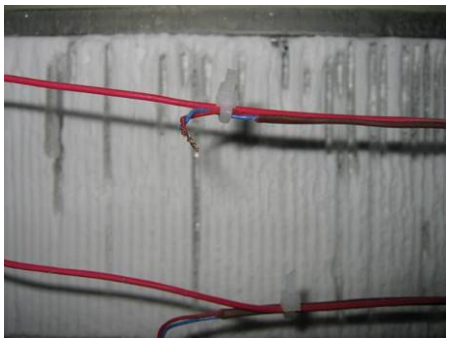

5h

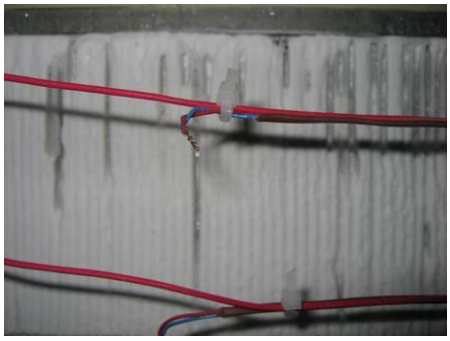

6h

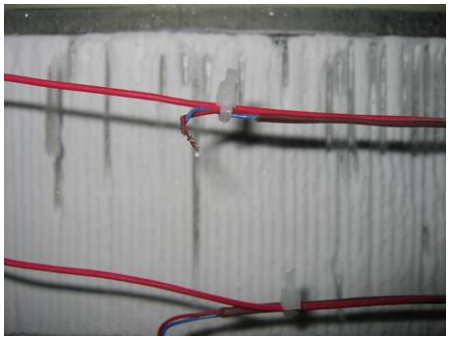

6.5h

Figure 34: 3rd Frost Cycle – 210 cfm

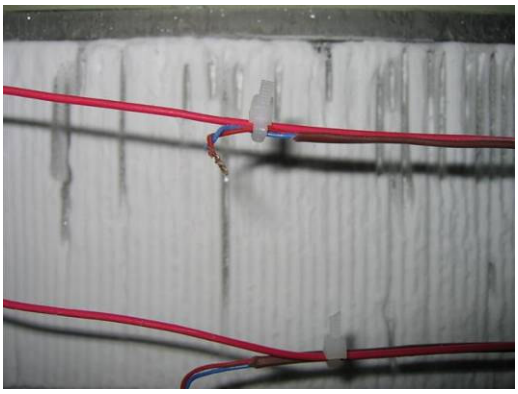

Start Defrost

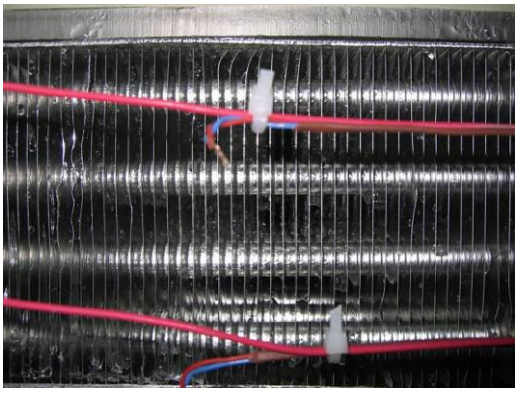

Heater Off – Compressor On

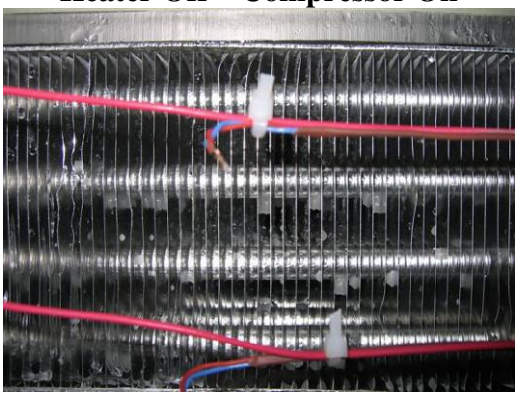

Fan On

Figure 35: 3rd Defrost Cycle – 210 cfm

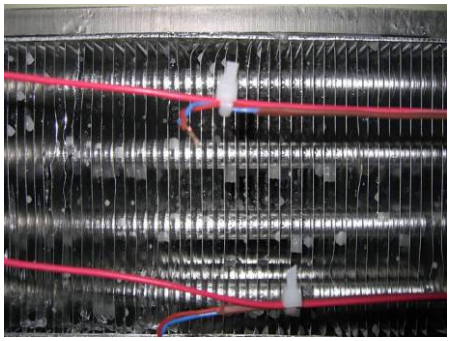

Startup

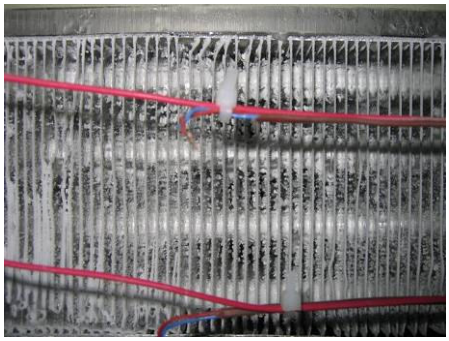

1h

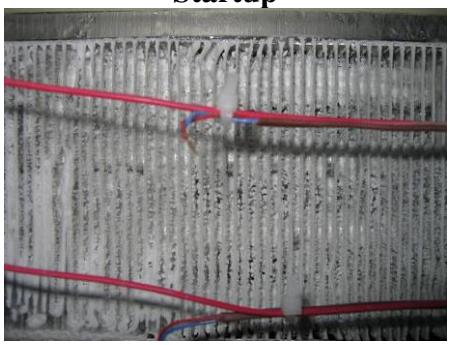

2h

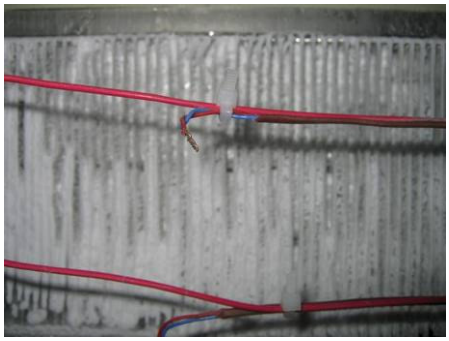

3h

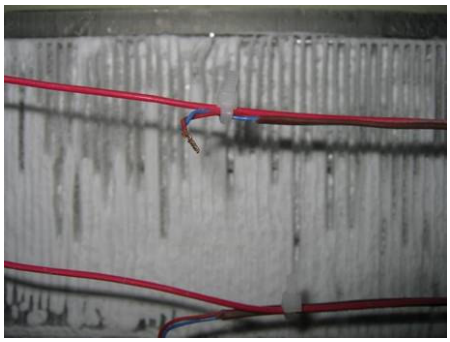

4h

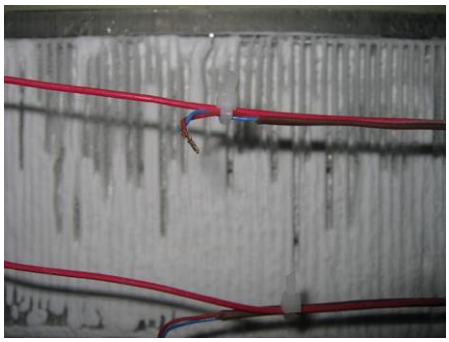

5h

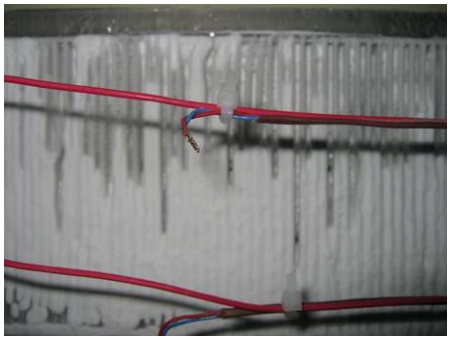

6h

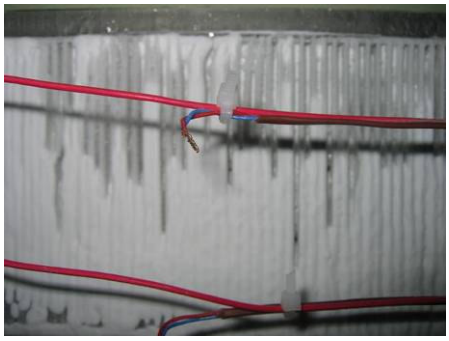

6.5h

Figure 36: 4th Frost Cycle – 210 cfm

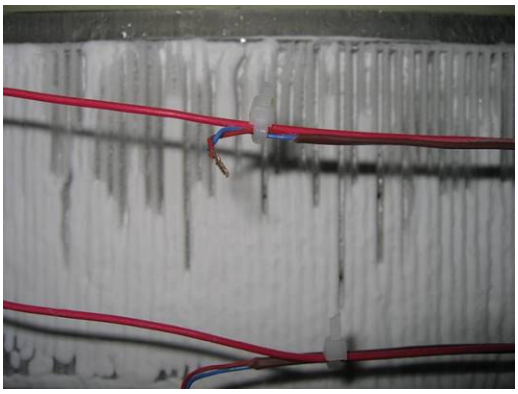

Start Defrost

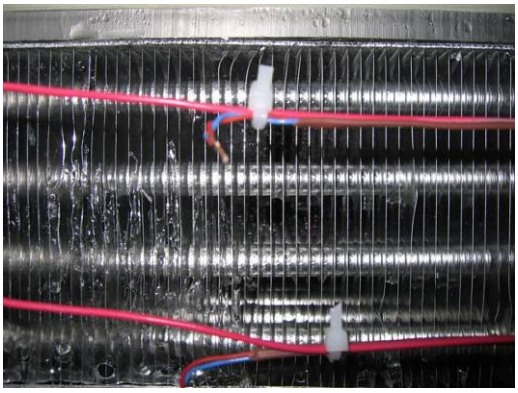

Heater Off – Compressor On

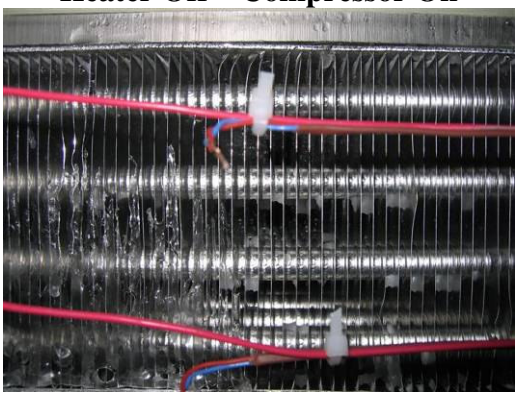

Fan On

Figure 37: 4th Defrost Cycle – 210 cfm

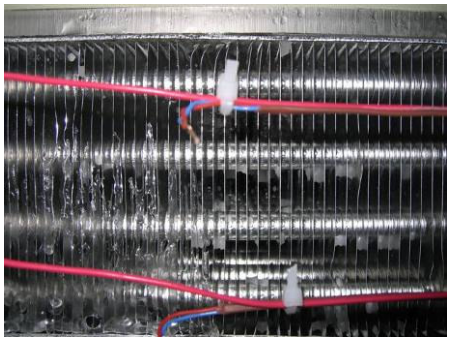

Startup

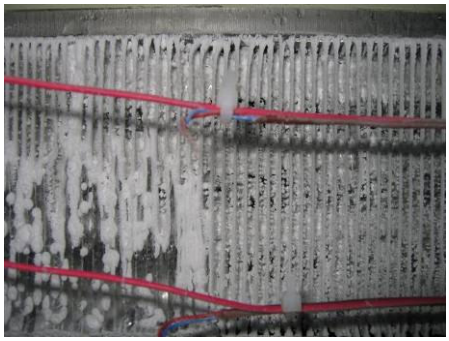

1h

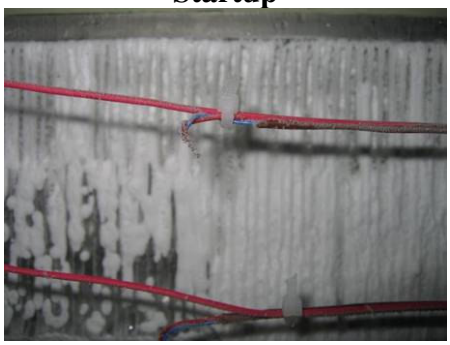

2h

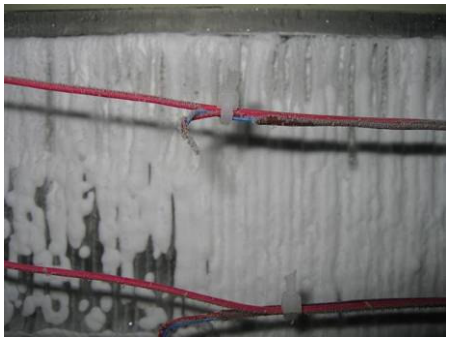

3h

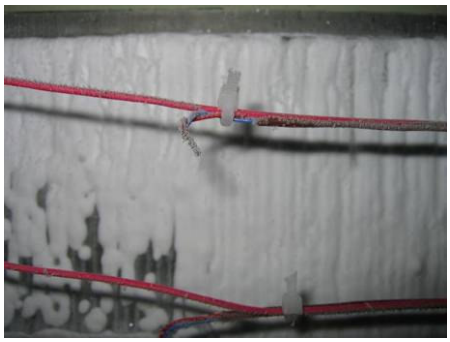

4h

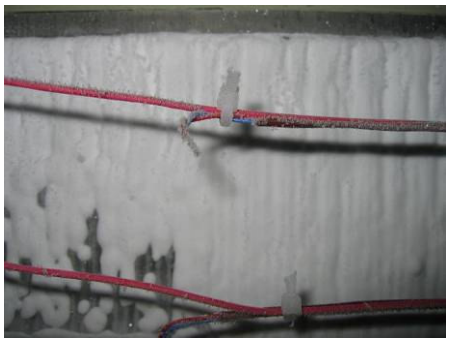

5h

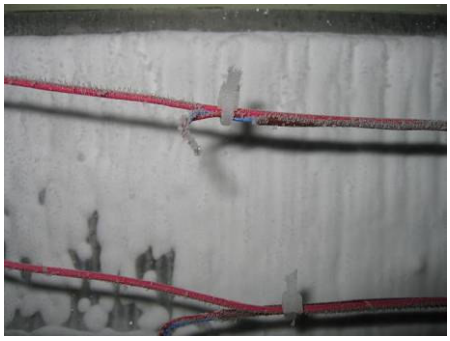

6h

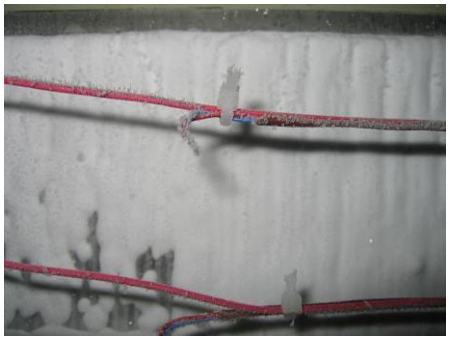

6.5h

Figure 38: 5th Frost Cycle – 210 cfm

Start Defrost

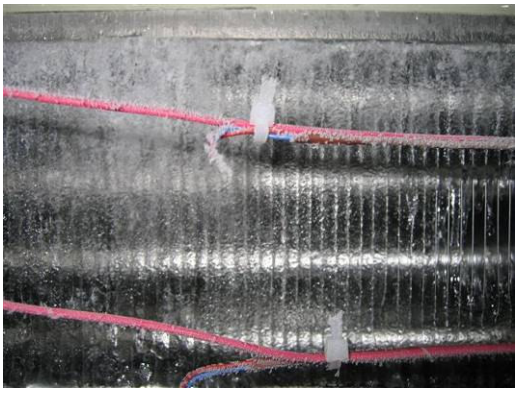

Heater Off – Compressor On

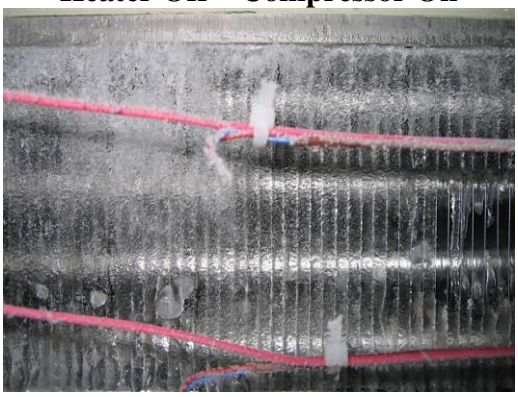

Fan On

Figure 39: 5th Defrost Cycle – 210 cfm

6.2 *Fin and Tube Type Heat Exchanger – 240 cfm*

This test was done with the specified test conditions with an air flow rate of 240 cfm. It was conducted for two frosting and defrosting cycles. The following figure shows the refrigerant side temperatures.

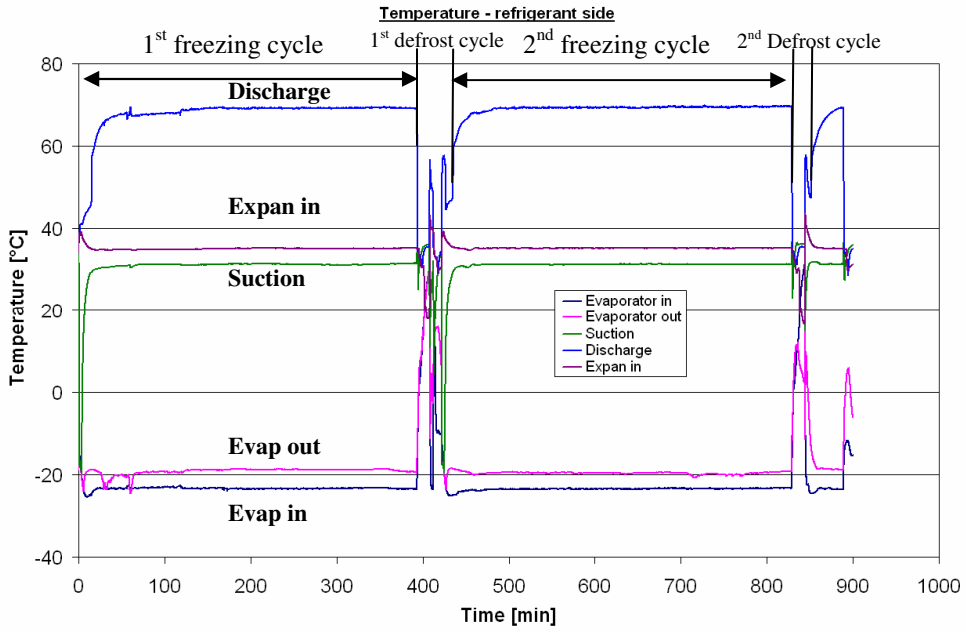

Figure 40: Refrigerant-Side Temperature versus Time at 240 cfm

It is obvious that the first defrost cycle differs from the second. This is to explain with a malfunction of the automatic defrost control. It started twice in a row, which shows in a spark in temperature and then a decrease. Since the compressor gets hot quickly it takes time to restart it. This explains the time delay before the startup of the second cycle.

The following figure shows the air side temperatures of all installed thermocouple grids.

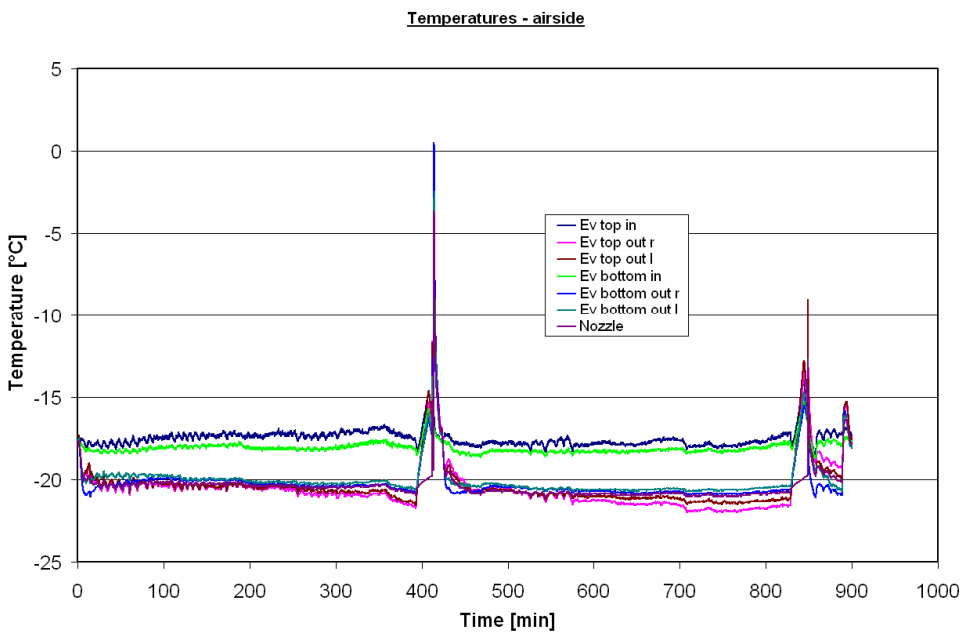

Figure 41: Evaporator Air-Side Temperature versus Time at 240 cfm

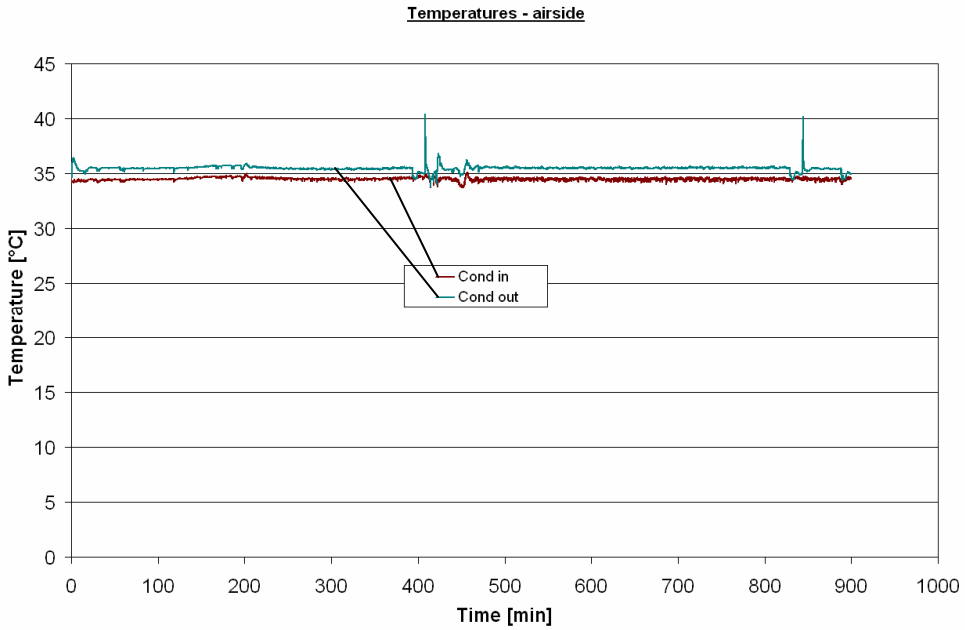

Figure 42: Condenser Air-Side Temperature versus Time at 240 cfm

Figure 42 shows the condenser inlet and outlet temperature. For the first cycle the inlet temperature is bouncing, but for the second cycle it is absolute constant. The pretest

was not as well performed as for the other test. It shows in the discharge pressure in Figure 43 at the startup, where additional adjustment was performed.

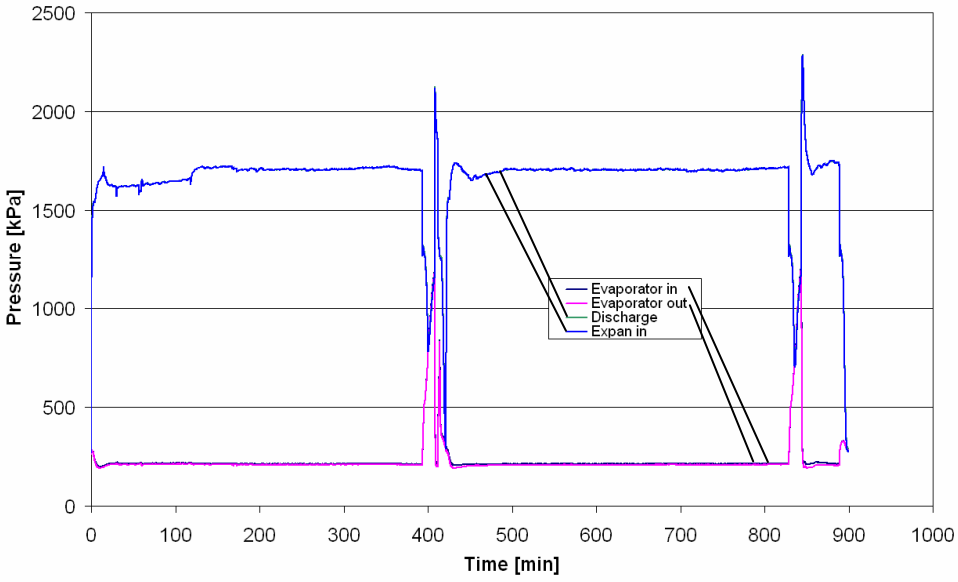

Figure 43: Pressure versus Time at 240 cfm

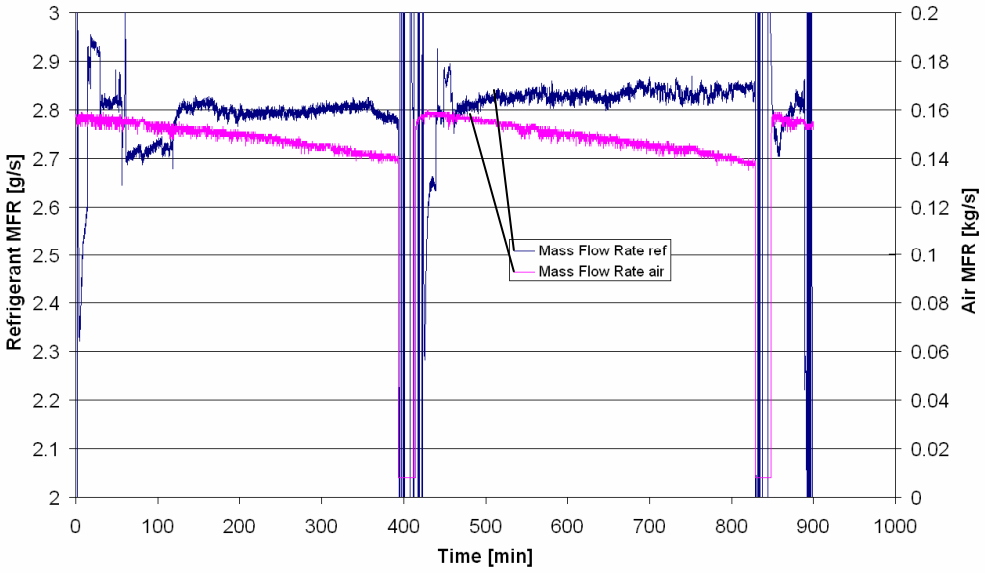

Figure 44: Mass Flow Rates versus Time at 240 cfm

Figure 44 shows the refrigerant side and air side mass flow rates. The adjustment at the beginning of the first cycle is obvious. The mass flow rate makes big jumps about 0.1 g/s until it becomes steady. At the startup of the second cycle the mass flow rate was not adjusted. This behavior is the usual startup until the compressor becomes steady.

The humidity level for the inlet and outlet of the coil is shown in Figure 45. The control was not as good as for the test at 210 cfm. The difference is a setup change from adjusting the humidity of the complete environmental chamber, shown here, and a local humidification used in the test at 210 cfm.

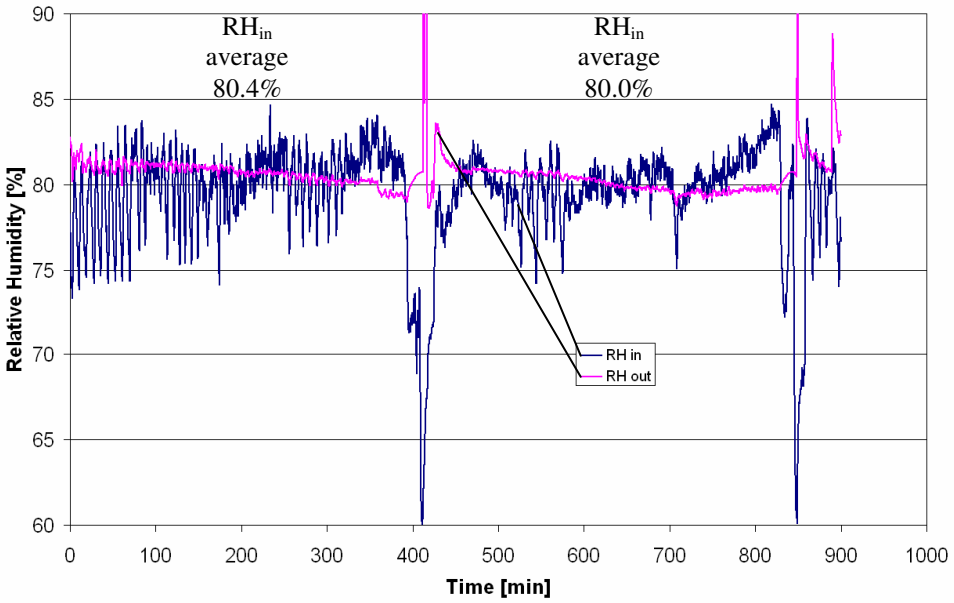

Figure 45: Relative Humidity versus Time at 240 cfm

The following figure shows the air side and refrigerant side differential pressure and the air flow rate across the coil. The graph shows ideal behavior, air side pressure drop constantly increasing, refrigerant side pressure drop after adjustment constant and air flow rate constantly decreasing.

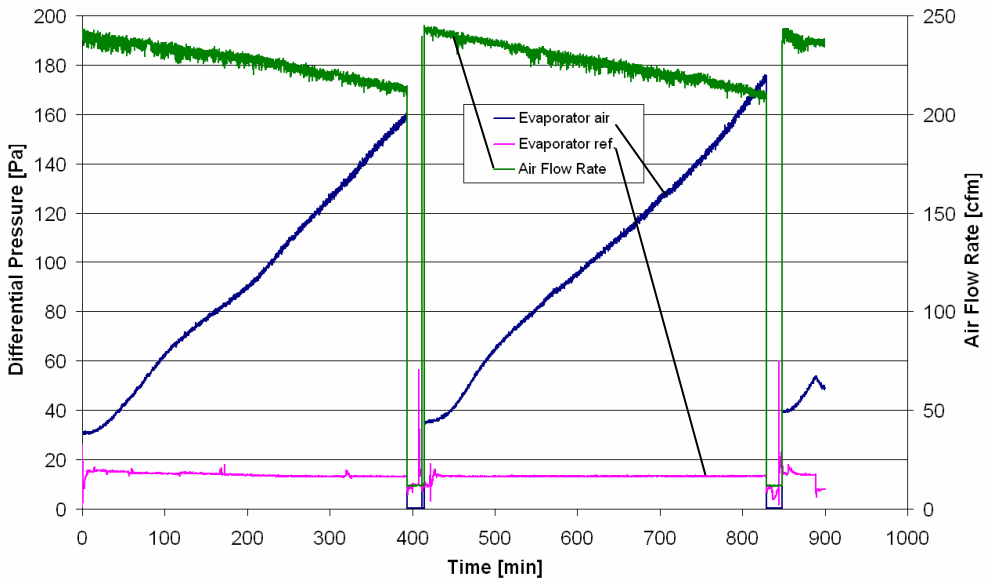

Figure 46: Differential Pressure and Air Flow rate versus Time at 240 cfm

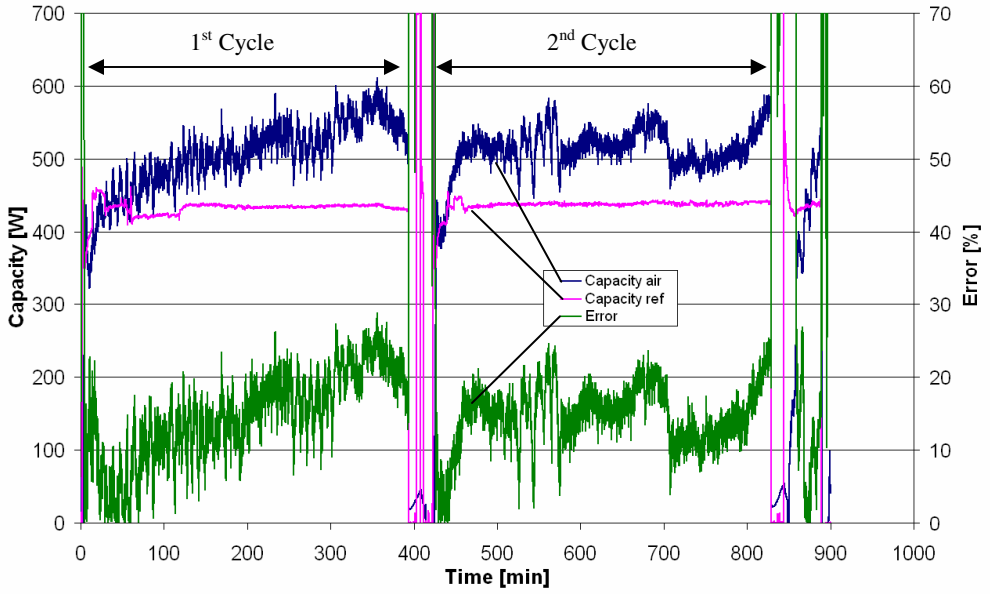

Figure 47: Capacity and Error versus Time at 240 cfm

Since the relative humidity was much more instable the capacity calculation was influenced too. That is why in Figure 47 the error goes up to 25%. The refrigerant side

capacity is the more reliable in this case. Figure 48 shows the superheat and sub cooling of the system. During first adjustment the superheat goes to zero, but then raises back.

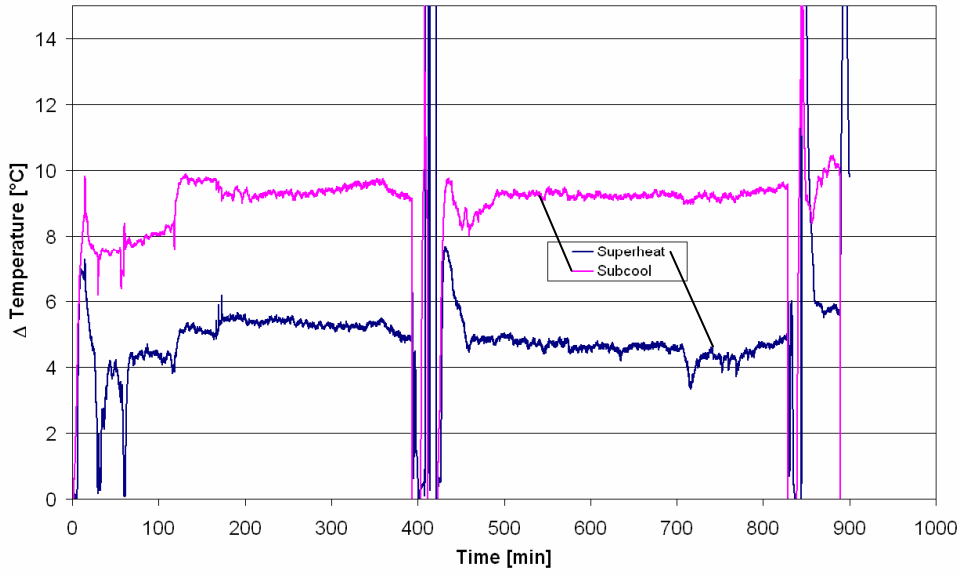

Figure 48: Degrees of Superheating and Subcooling versus Time at 240 cfm

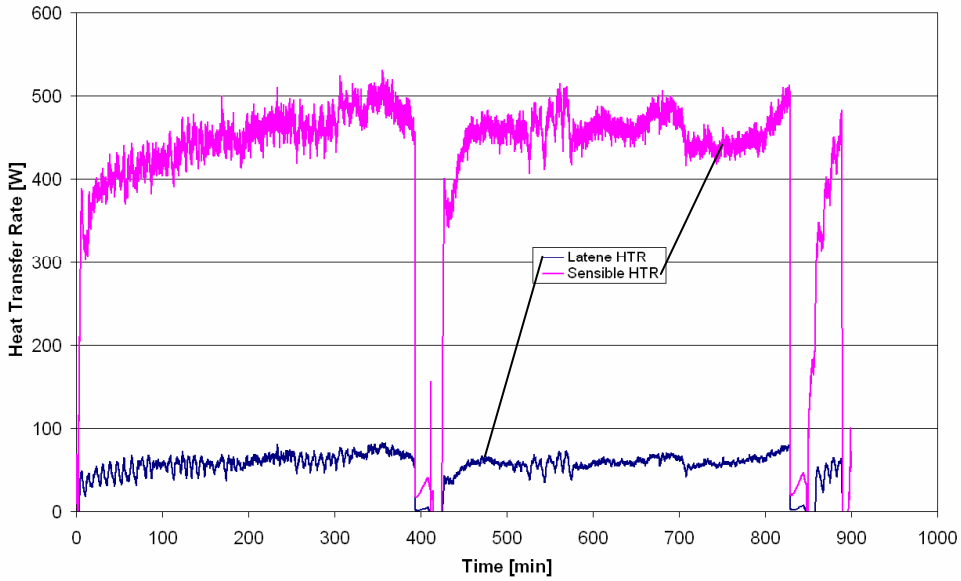

Figure 49: Sensible and Latent Heat Transfer Rate versus Time at 240 cfm

The sensible and latent heat transfer rate is shown in Figure 49. Although the relative humidity made major jumps the latent heat transfer rates is about the same.

Figure 50 shows the defrost heater power consumption and the refreeze delay time control.

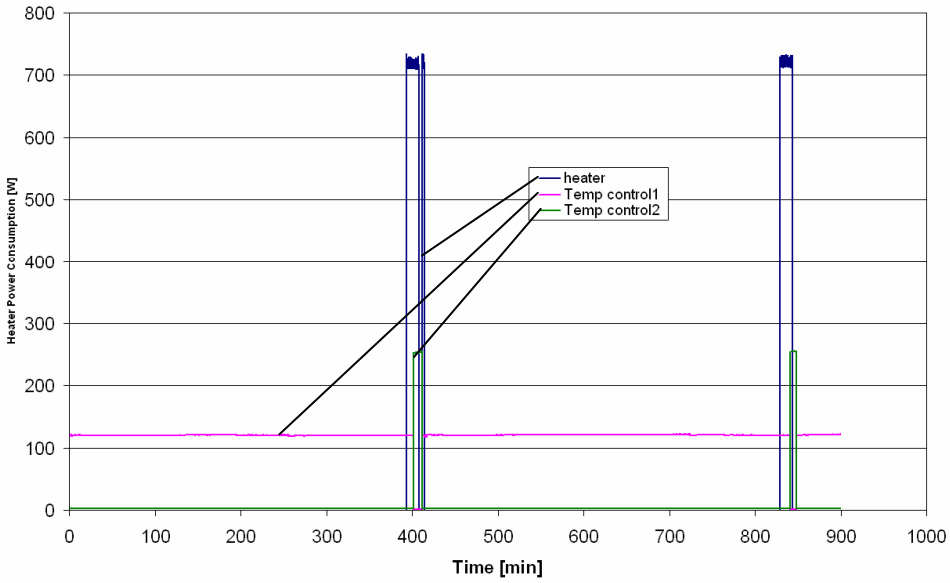

Figure 50: Heater Power Consumption versus Time at 240 cfm

The following Figures 51 to 54 show pictures taken at the inlet of the coil. All two freezing and defrosting cycles are shown in detail. Especially focus should be set for the startup picture of each freezing cycle, since the coil never drains completely and water refreezes.

Figure 51 shows the first frosting cycle of the evaporator for 240 cfm. The initial crystal growth on the surface is very similar to the test at 210 cfm. The difference is in the continuation of the frost growth. The crystals do not grow as big as with the lower air flow rate. Moreover even at the end of the cycle, the surface is barely covered completely.

Figure 52 shows the first defrost cycle. The first picture is the startup of the defrost cycle, when the heater turns on. The second picture shows the turning point from heating the evaporator to re-cooling the evaporator. The third picture shows the refrozen water on the evaporator shifting back to normal freezing cycle mode. All over the amount of water seems to be comparable to the first defrosting cycle at 210 cfm.

Figure 53 shows the second frosting cycle. The frost growth happens much faster compared to the first cycle and the complete surface is covered with ice crystals. Also the surface roughness seems to be much higher than for the first cycle. The higher surface roughness enhances the heat transfer and makes up for the additional thermal resistance of the frost layer. This is the explanation why the capacity of the evaporator did not decrease much even with increased frost formation.

Figure 54 shows the second defrost cycle. Outstanding is the re-cooled coil. It seems that much more ice is accumulated after the second defrost cycle.

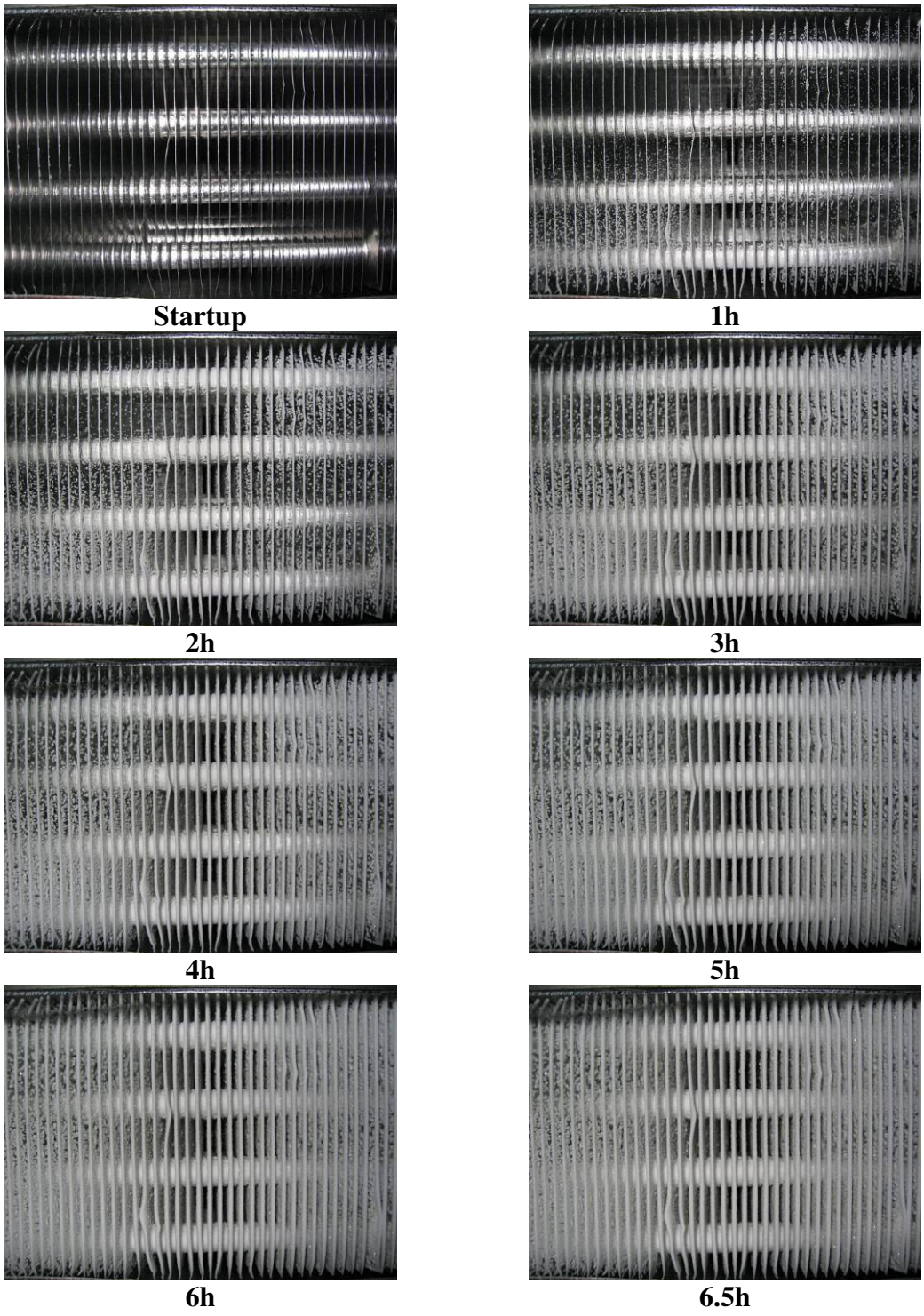

Figure 51: 1st Frost Cycle – 240 cfm

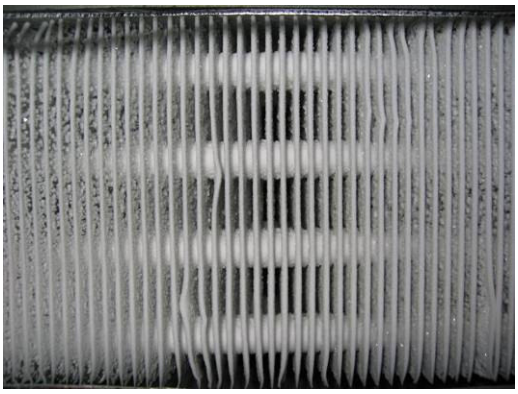

Start Defrost

Heater Off – Compressor On

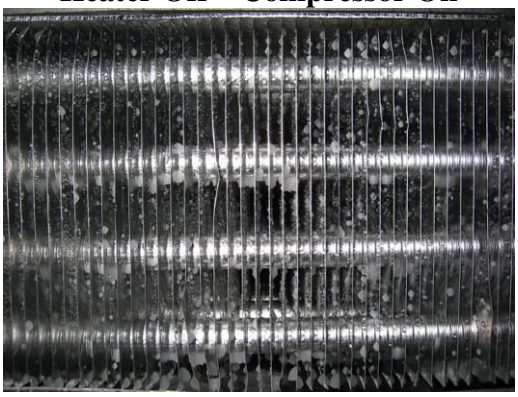

Fan On

Figure 52: 1st Defrost Cycle – 240 cfm

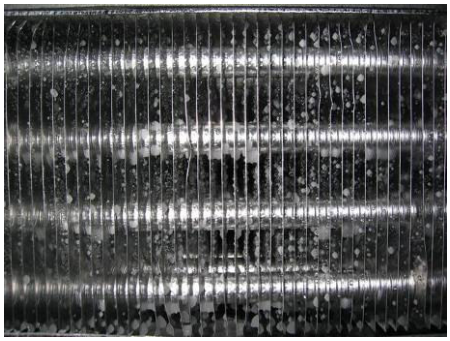

Startup

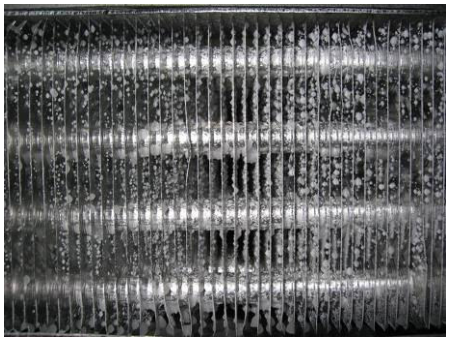

1h

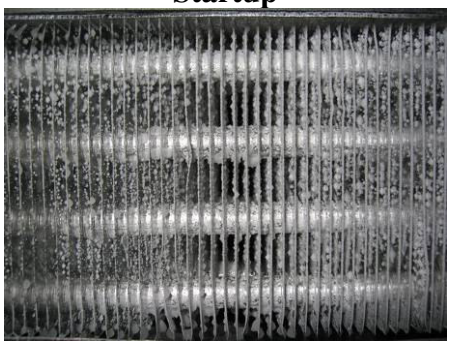

2h

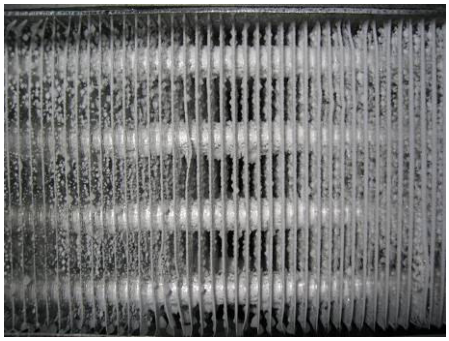

3h

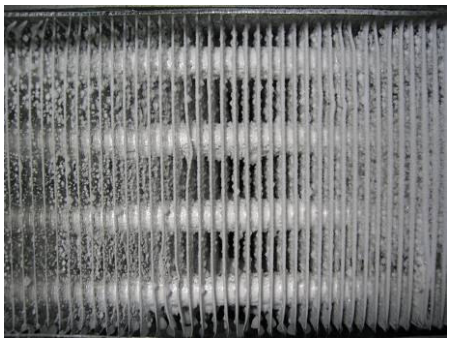

4h

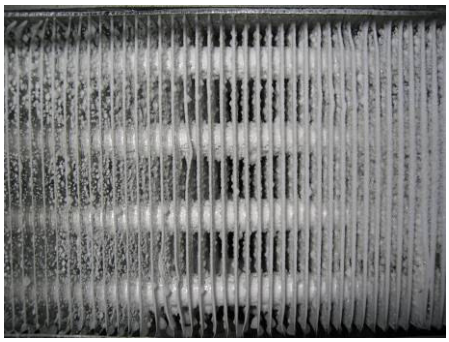

5h

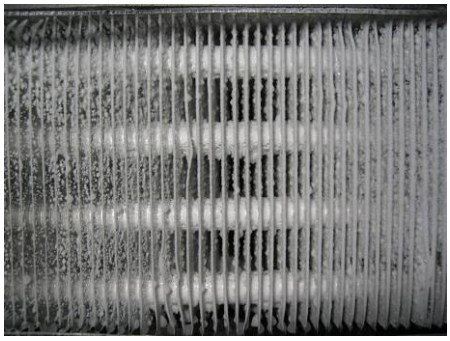

6h

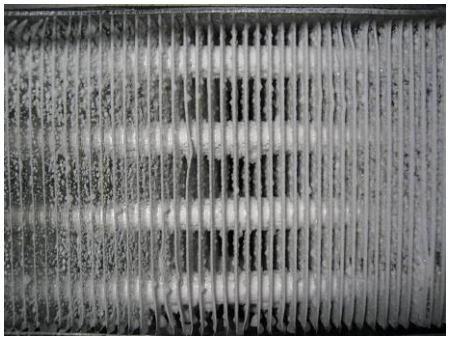

6.5h

Figure 53: 2nd Frost Cycle – 240 cfm

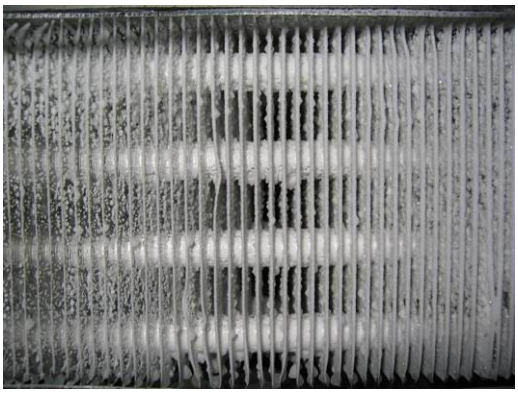

Start Defrost

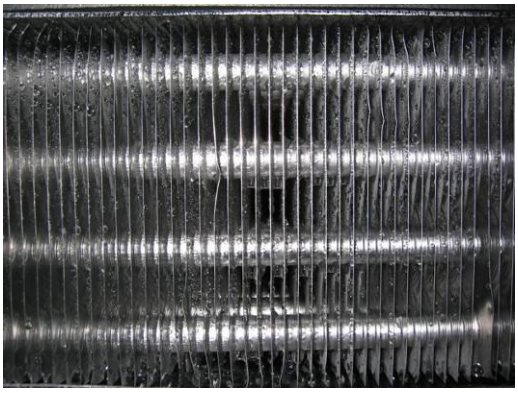

Heater Off – Compressor On

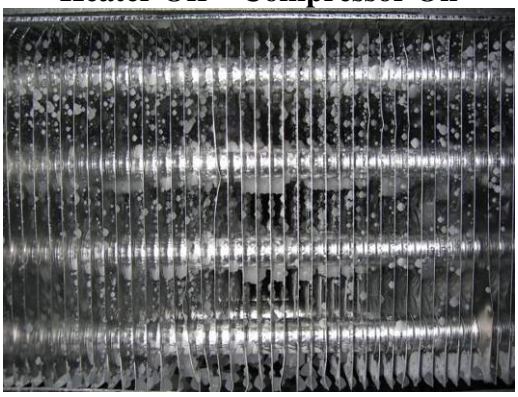

Fan On

Figure 54: 2nd Defrost Cycle – 240 cfm

6.3 Comparison and Discussion

The conducted tests produced a lot of data. Therefore it is necessary to find a way to compare the individual cycles. At every start of a new cycle the compressor needs about 45 min to come to steady state, which means its discharge temperature increases to a maximum. During this warm-up period the system pressure shifts slightly up. Once the discharge temperature reaches its steady state, the system pressures stabilize too. Therefore the first 45 min of each cycle is not valid for comparison. However, the data after the first hour to the end of the freezing cycle should be valid for a fair comparison. Since frost formation occurs continuously the test is always transient and the total average over the cycle period does not make sense for all variables. Also single point would not be a good comparison and not accurate at all. Therefore a ten minute time period at one hour and after 6.5 hours as well as the total average from one hour to 6.5 hours of each cycle was chosen. In order to better understand which three numbers are compared, the averaging time periods are indicated in Figure 55.

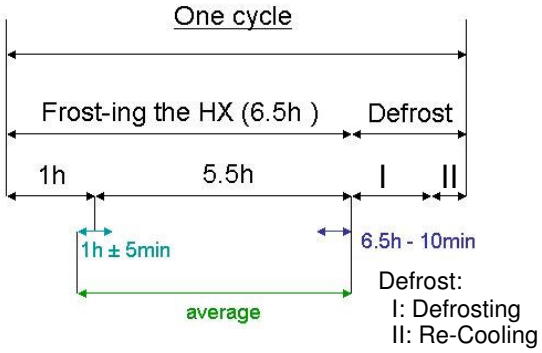

Figure 55: Comparison Time Ranges

After evaluating each test cycle with the pattern described above, the cycles can be compared. The most important variable is the relative humidity at the inlet, since it

determined how much water vapor will be carried into the coil. Therefore, the following table shows the average relative humidity of each cycle for the conducted tests.

Table 14: $RH_{average\ inlet}$ Comparison

Test	Cycle	$RH_{average\ inlet}$
210 cfm	1	77.9
	2	77.8
	3	79.1
	4	79.5
	5	80.5
240 cfm	1	80.4
	2	80.0

Since the fifth cycle of the test at 210 cfm, as seen in the pictures, had frost at the inlet at its start, it is not a valid for comparison. Cycle three and four at 210 cfm and cycle one and two at 240 cfm show a comparable relative humidity level. The completely analyzed data of cycle three and four at 210 cfm and cycle one and two at 240 cfm is shown in the appendix in Table 17 and Table 18.

In order to be able to see how well the tests compare with each other, the system measurements after one hour of the freezing cycle should fit to the original test conditions. The comparison of the cycles with comparable relative humidity is shown in Table 15.

Table 15: Cycle Comparison at 1h

Nom. AFR	Cycle	$T_{ev\ in}$ Ref [°C]	$T_{exp\ in}$ Ref [°C]	$T_{ev\ in}$ Air [°C]	MFR Ref [g/s]	AFR [cfm]	Super Heat [°C]	Sub cool [°C]	Cap. Ref [W]
210cfm (100%)	3	-23.5	35.1	-17.8	2.4	191.1 (91.0%)	5.2	8.2	375.9
210cfm (100%)	4	-23.3	35.2	-17.7	2.4	196.2 (93.4%)	4.7	7.9	372.7
240cfm (100%)	1	-23.2	34.8	-18.0	2.8	236.2 (98.4%)	2.3	7.5	424.7
240cfm (100%)	2	-23.7	35.2	-18.0	2.8	237.7 (99.0%)	4.9	8.9	435.7
Test cond.		**-23.3**	**35.0**	**-17.8**	*	*	**4.5**	**8.3**	*

* Values adjusted in pretest or calculated

The fourth cycle at 210cfm and the second cycle at 240cfm fit together the best, not only because of the fitting data, but also in terms of cycling. Both of them have a defrost cycle before they start, which provides them the about same start up conditions. A big difference happened in the reduction of the air flow rate within the first hour, as shown in Table 15. For the cycle four at 210 cfm it reduced already about 6.6% while it only decreased about 1.0% for the second cycle at 240 cfm.

However, it is possible to investigate the effect of an increased air flow rate for the rest of the cycle. The frost buildup observed from the pictures is much more for 210 cfm than for 240 cfm. This fact is also deserved in the outlet relative humidity. By comparing the humidity ratios of the inlet and outlet conditions it shows that the frost buildup and therefore humidity ratio reduction is less for the test at 240 cfm. The analysis is shown in Table 16.

Table 16: Humidity Ratio Comparison

Nom. AFR	Cycle	$RH_{average\ inlet}$ [%]	T_{in} [°C]	$RH_{average\ outlet}$ [%]	T_{nozzle} [°C]
210 cfm	4	79.5	-17.7	74.5	-20.9
240 cfm	2	80.0	-18.0	80.1	-20.5
		Humidity Ratio		**Humidity Ratio**	
210 cfm	4	0.0006302		0.0004364	
240 cfm	2	0.0006165		0.0004877	
		Difference			
210 cfm	4	0.0001938			
240 cfm	2	0.0001288			
		Air side MFR [kg/s]			
210 cfm	4	0.112			
240 cfm	2	0.148			
		Frost Amount (6.5h) [kg]			
210 cfm	4	0.507			
240 cfm	2	0.446 (12.1% less)			

The humidity ratio at the inlet and outlet was calculated with temperature, relative humidity and pressure. The difference in humidity ratio multiplied by average air side mass flow rate and the cycle time gives the theoretical frost amount on the coil at the end of the cycle. The difference in frost amount is about 12.1%, although the test conditions, except the air flow rate, for the coil were the same. The air flow rate was increased from 210 cfm to 240 cfm, an increase of 14.3%. Therefore the increased air flow rate must increase the density of frost deposition on the coil, since less blockage of the air passage at the coil is visible. This effect was also investigated by R. Yun et al. [4].

7 Conclusion

The purpose of this study was to design, size, construct, calibrate and run a test stand to investigate the evaporator frost performance for low temperature applications. The test system is designed to test any type of small capacity evaporator, whose outer dimensions do not exceed 20" height by 25" width. The refrigeration system consists out four components, a compressor, condenser, evaporator and expansion valve. All components are easy accessible and changeable in order to test different kind of refrigerant or capacity range. The data acquisition control can handles manual or fully automatic defrost control. The automatic defrost control can be adjusted for an individual best fit for the heat exchanger.

Pretests and tests were conducted for specific test conditions at two air flow rates for at least two cycles. During the freezing cycle pictures were taken each 15 min. For the defrost cycle pictures each minute and real time movie were recorded. Pictures and movies were recorded for the inlet as well as the outlet of the heat exchanger in order to visually investigate the frosting behavior of the heat exchanger. The data was recorded in every five seconds and the datasets of each test includes the compressor's mass flow rate, the defrost heaters power consumption, temperatures and pressures at each state point for air- as well as refrigerant-side. The tests have shown that the system is able to accomplish all desired test conditions.

Tests were conducted for the two air flow rates. The data was recorded and compared. The performance of the evaporator was evaluated continuously during testing. Its performance degraded constantly by accumulation of frost during each frosting cycle, which increased the thermal resistance and blocked the air passage through the coil. This

resulted in the loss of superheat towards the end of each cycle. The defrost operation could not restore the full capacity of the evaporator. The defrost cycle consists out of two phases, melting the ice and re-cooling the coil. The first phase melts all the ice of the coil but the drainage of the resulting water is incomplete. The re-cooling phase freezes the amount of water residue on the evaporator coil, which causes an accelerated frost formation in the following freezing cycle. All over this behavior causes an accelerated reduction in evaporator capacity and therefore earlier superheat loss.

To compare the cycles with two different air flow rates, the most suitable ones were chosen. The decision was based on the air inlet conditions of the coil such as relative humidity and temperature and as well the refrigerant side inlet conditions such as evaporator and condenser temperature and pressure. Two cycles had a tight fit and were compared to investigate the effect of an increased air flow rate. It showed that the frost amount of the cycle at 240 cfm was 12.1% less. The air flow rate change is about 14.3% from 210 cfm to 240 cfm. There are two explanations for this behavior. First of all has been investigated in earlier research that an increased air flow rate increases the density of the frost, which results in less blockage of the air gap. And if the frost does not build up a net of interconnections from one surface to another, the total amount of frost formation is limited. Therefore the observed frost formation happens.

8 Future Work

The test results of various operating conditions showed that the behavior of the coil under frosting conditions can not determine easily and it needs to be further explored.

The future work should include

- An detailed investigation of the driving forces for frost formation for a better analysis
- The effect of the relative humidity has to be investigated over the whole range.
- More test with different types of fins.
- More test with different types of heat exchanges.
- Comparison and further development of models to predict freezing of the coil

9 Appendix

Table 17: Test results for 210 cfm – Cycle 3 and 4

HX Comparison Wind Tunnel Test - Overview								
HX	**Test**	**Phase**	**air/ref side**	**Measurement**	**Unit**	**Frost 1/2 - Time**		
						at 1h ± 5min	**at 6.5h - 10min**	**1- 6.5h average**
Benchmark	Test 17	5. Frost 3 c	ref side	T evap in	°C	-23.6	-24.0	-23.8
Benchmark	Test 17	5. Frost 3 c	ref side	T evap out	°C	-18.8	-24.0	-20.2
Benchmark	Test 17	5. Frost 3 c	ref side	T suction	°C	32.4	32.3	32.4
Benchmark	Test 17	5. Frost 3 c	ref side	T discharge	°C	67.6	68.0	67.9
Benchmark	Test 17	5. Frost 3 c	ref side	T cond out	°C	35.1	35.2	35.1
Benchmark	Test 17	5. Frost 3 c	air side	T evap in	°C	-17.8	-17.7	-17.7
Benchmark	Test 17	5. Frost 3 c	air side	T evap out	°C	-20.5	-21.4	-21.1
Benchmark	Test 17	5. Frost 3 c	air side	T nozzle	°C	-20.2	-21.0	-20.6
Benchmark	Test 17	5. Frost 3 c	air side	T cond in	°C	34.9	35.0	35.0
Benchmark	Test 17	5. Frost 3 c	air side	T cond out	°C	35.9	36.1	36.0
Benchmark	Test 17	5. Frost 3 c	ref side	P cond out	kPa	1656.9	1651.3	1654.7
Benchmark	Test 17	5. Frost 3 c	ref side	P evap in	kPa	217.5	214.5	215.9
Benchmark	Test 17	5. Frost 3 c	ref side	P evap out	kPa	210.0	208.4	208.8
Benchmark	Test 17	5. Frost 3 c	ref side	MFR	g/s	2.4	2.4	2.4
Benchmark	Test 17	5. Frost 3 c	air side	AFR	cfm	191.3	142.7	169.9
Benchmark	Test 17	5. Frost 3 c	air side	RH in	%	78.5	79.3	79.1
Benchmark	Test 17	5. Frost 3 c	air side	RH out	%	75.4	74.1	74.6
Benchmark	Test 17	5. Frost 3 c	ref side	Dp	kPa	12.0	11.6	11.8
Benchmark	Test 17	5. Frost 3 c	air side	Dp	Pa	50.9	241.5	142.1
Benchmark	Test 17	5. Frost 3 c	ref side	superheat	°C	5.2	0.1	3.9
Benchmark	Test 17	5. Frost 3 c	ref side	subcool	°C	8.2	7.9	8.0
Benchmark	Test 17	5. Frost 3 c	ref side	Capacity	W	375.9	340.6	370.3
Benchmark	Test 17	5. Frost 3 c	air side	Capacity	W	370.7	369.3	390.8
Benchmark	Test 17	6. Defrost 3 c						
Benchmark	Test 17	7. Frost 4 c	ref side	T evap in	°C	-23.3	-23.8	-23.5
Benchmark	Test 17	7. Frost 4 c	ref side	T evap out	°C	-18.9	-24.0	-20.8
Benchmark	Test 17	7. Frost 4 c	ref side	T suction	°C	32.6	31.8	32.3
Benchmark	Test 17	7. Frost 4 c	ref side	T discharge	°C	68.4	68.0	68.2
Benchmark	Test 17	7. Frost 4 c	ref side	T cond out	°C	35.2	35.0	35.1
Benchmark	Test 17	7. Frost 4 c	air side	T evap in	°C	-17.7	-17.6	-17.7
Benchmark	Test 17	7. Frost 4 c	air side	T evap out	°C	-20.4	-21.6	-21.0
Benchmark	Test 17	7. Frost 4 c	air side	T nozzle	°C	-20.2	-20.9	-20.5
Benchmark	Test 17	7. Frost 4 c	air side	T cond in	°C	35.0	34.8	34.9
Benchmark	Test 17	7. Frost 4 c	air side	T cond out	°C	36.0	35.6	35.8
Benchmark	Test 17	7. Frost 4 c	ref side	P cond out	kPa	1650.4	1630.0	1643.0
Benchmark	Test 17	7. Frost 4 c	ref side	P evap in	kPa	220.4	216.2	218.7
Benchmark	Test 17	7. Frost 4 c	ref side	P evap out	kPa	213.0	210.4	212.0
Benchmark	Test 17	7. Frost 4 c	ref side	MFR	g/s	2.4	2.4	2.4
Benchmark	Test 17	7. Frost 4 c	air side	AFR	cfm	196.2	138.8	170.3
Benchmark	Test 17	7. Frost 4 c	air side	RH in	%	78.4	79.8	79.5
Benchmark	Test 17	7. Frost 4 c	air side	RH out	%	75.0	73.9	74.5
Benchmark	Test 17	7. Frost 4 c	ref side	Dp	kPa	11.9	11.4	11.7
Benchmark	Test 17	7. Frost 4 c	air side	Dp	Pa	52.0	259.1	158.4
Benchmark	Test 17	7. Frost 4 c	ref side	superheat	°C	4.7	0.0	2.9
Benchmark	Test 17	7. Frost 4 c	ref side	subcool	°C	7.9	7.6	7.8
Benchmark	Test 17	7. Frost 4 c	ref side	Capacity	W	372.7	-175.0	259.8
Benchmark	Test 17	7. Frost 4 c	air side	Capacity	W	406.6	354.3	399.3
Benchmark	Test 17	8. Defrost 4 c						

Table 18: Test results for 240 cfm – Cycle 1 and 2

HX Comparison Wind Tunnel Test - Overview								
HX	**Test**	**Phase**	**air/ref side**	**Measurement**	**Unit**	**Frost 1/2 - Time**		
						at 1h ± 5min	**at 6.5h - 10min**	**1- 6.5h average**
Benchmark 240cfm	Test 05	1. Frost 1	ref side	T evap in	°C	-23.2	-23.4	-23.3
Benchmark 240cfm	Test 05	1. Frost 1	ref side	T evap out	°C	-21.5	-19.3	-19.0
Benchmark 240cfm	Test 05	1. Frost 1	ref side	T suction	°C	30.9	31.5	31.3
Benchmark 240cfm	Test 05	1. Frost 1	ref side	T discharge	°C	67.7	69.2	68.9
Benchmark 240cfm	Test 05	1. Frost 1	ref side	T cond out	°C	34.8	35.2	35.1
Benchmark 240cfm	Test 05	1. Frost 1	air side	T evap in	°C	-18.0	-17.7	-17.7
Benchmark 240cfm	Test 05	1. Frost 1	air side	T evap out	°C	-20.1	-21.0	-20.4
Benchmark 240cfm	Test 05	1. Frost 1	air side	T nozzle	°C	-20.4	-20.8	-20.4
Benchmark 240cfm	Test 05	1. Frost 1	air side	T cond in	°C	34.4	34.6	34.5
Benchmark 240cfm	Test 05	1. Frost 1	air side	T cond out	°C	35.4	35.5	35.5
Benchmark 240cfm	Test 05	1. Frost 1	ref side	P cond out	kPa	1621.9	1706.3	1697.0
Benchmark 240cfm	Test 05	1. Frost 1	ref side	P evap in	kPa	215.2	212.1	213.5
Benchmark 240cfm	Test 05	1. Frost 1	ref side	P evap out	kPa	210.8	208.0	209.3
Benchmark 240cfm	Test 05	1. Frost 1	ref side	MFR	g/s	2.8	2.8	2.8
Benchmark 240cfm	Test 05	1. Frost 1	air side	AFR	cfm	236.2	213.6	225.7
Benchmark 240cfm	Test 05	1. Frost 1	air side	RH in	%	79.2	81.1	80.4
Benchmark 240cfm	Test 05	1. Frost 1	air side	RH out	%	81.1	79.4	80.6
Benchmark 240cfm	Test 05	1. Frost 1	ref side	Δp	kPa	14.8	13.1	13.7
Benchmark 240cfm	Test 05	1. Frost 1	air side	Δp	Pa	45.7	156.6	100.4
Benchmark 240cfm	Test 05	1. Frost 1	ref side	superheat	°C	2.3	4.9	5.0
Benchmark 240cfm	Test 05	1. Frost 1	ref side	subcool	°C	7.5	9.2	9.1
Benchmark 240cfm	Test 05	1. Frost 1	ref side	Capacity	W	424.7	431.8	432.9
Benchmark 240cfm	Test 05	1. Frost 1	air side	Capacity	W	456.4	541.6	517.5
Benchmark 240cfm	Test 05	2. Defrost 1						
Benchmark 240cfm	Test 05	3. Frost 2	ref side	T evap in	°C	-23.7	-23.3	-23.4
Benchmark 240cfm	Test 05	3. Frost 2	ref side	T evap out	°C	-19.6	-19.4	-19.7
Benchmark 240cfm	Test 05	3. Frost 2	ref side	T suction	°C	31.3	31.3	31.3
Benchmark 240cfm	Test 05	3. Frost 2	ref side	T discharge	°C	68.9	69.7	69.4
Benchmark 240cfm	Test 05	3. Frost 2	ref side	T cond out	°C	35.2	35.2	35.2
Benchmark 240cfm	Test 05	3. Frost 2	air side	T evap in	°C	-18.0	-17.7	-18.0
Benchmark 240cfm	Test 05	3. Frost 2	air side	T evap out	°C	-20.4	-21.0	-20.9
Benchmark 240cfm	Test 05	3. Frost 2	air side	T nozzle	°C	-20.7	-20.8	-20.9
Benchmark 240cfm	Test 05	3. Frost 2	air side	T cond in	°C	34.5	34.5	34.5
Benchmark 240cfm	Test 05	3. Frost 2	air side	T cond out	°C	35.6	35.6	35.5
Benchmark 240cfm	Test 05	3. Frost 2	ref side	P cond out	kPa	1692.4	1711.9	1705.4
Benchmark 240cfm	Test 05	3. Frost 2	ref side	P evap in	kPa	211.4	213.8	212.8
Benchmark 240cfm	Test 05	3. Frost 2	ref side	P evap out	kPa	205.9	208.9	207.7
Benchmark 240cfm	Test 05	3. Frost 2	ref side	MFR	g/s	2.8	2.8	2.8
Benchmark 240cfm	Test 05	3. Frost 2	air side	AFR	cfm	237.7	212.3	224.9
Benchmark 240cfm	Test 05	3. Frost 2	air side	RH in	%	81.2	82.5	80.0
Benchmark 240cfm	Test 05	3. Frost 2	air side	RH out	%	80.9	79.8	80.1
Benchmark 240cfm	Test 05	3. Frost 2	ref side	Δp	kPa	13.2	13.3	13.3
Benchmark 240cfm	Test 05	3. Frost 2	air side	Δp	Pa	56.5	165.3	109.2
Benchmark 240cfm	Test 05	3. Frost 2	ref side	superheat	°C	4.9	4.7	4.6
Benchmark 240cfm	Test 05	3. Frost 2	ref side	subcool	°C	8.9	9.4	9.2
Benchmark 240cfm	Test 05	3. Frost 2	ref side	Capacity	W	435.6	441.4	438.6
Benchmark 240cfm	Test 05	3. Frost 2	air side	Capacity	W	521.6	534.7	516.8
Benchmark 240cfm	Test 05	4. Defrost 2						

10 References

[1] http://www.its.caltech.edu/~atomic/snowcrystals/

[2] N.H. Fletcher, The Chemical Physics of Ice, Cambridge University Press, Cambridge, 1970 (chapter 4 and 5)

[3] B. Na, R. L. Webb: A fundamental understanding of factors affecting frost nucleation, International Journal of Heat and Mass Transfer 46, 2003, pp. 3797-3808

[4] R. Yun, Y. Kim, M. Min: Modeling of frost growth and frost properties with airflow over a flat plate, International Journal of Refrigeration 25, 2002, pp.362-371

[5] D. Seker, H. Karatas, N. Egrican: Frost formation on fin- and-tube type heat exchangers. Part I-Modeling of frost formation on fin-and-tube heat exchangers, International Journal of Refrigeration 27, 2004, pp.367-374

[6] D. Seker, H. Karatas, N. Egrican: Frost formation on fin- and-tube type heat exchangers. Part II-Experimental Investigation of frost formation on fin-and-tube heat exchangers, International Journal of Refrigeration 27, 2004, pp.375-377

[7] Y. Xia, P. S. Hrnjak, A. M. Jacobi: An empirical study about frost accumulation effects on louvered-fin micro channel heat exchangers, International Refrigeration and Air Conditioning Conference, Purdue, July 12-15 2004

[8] H. Lee, J. Shin, S. Ha, B. Choi, J. Lee: Frost formation on a plate with different surface hydrophilicity, International Journal of Heat and Mass Transfer 47, 2004, pp.4881-4893

[9] Z. Liu, H. Wang, X. Zhang, S. Meng, C. Ma: An experimental study on minimizing frost deposition on a cold surface under natural convection conditions by the use of novel anti-frosting paint. Part I Anti frosting performance and comparison with the uncoated metallic surface, International Journal of Refrigeration 29, 2006, pp. 229-236

[10] Z. Liu, H. Wang, X. Zhang, S. Meng, C. Ma: An experimental study on minimizing frost deposition on a cold surface under natural convection conditions by the use of novel anti-frosting paint. Part II Long-term performance, frost layer observation and mechanism analysis, International Journal of Refrigeration 29, 2006, pp. 237-242

[11] ANSI/ASHRAE Standard 41.2 1987, Standard Methods for Laboratory Air-Flow Measurements

[12] ASHRAE, 2001, ASHRAE Handbook-Fundamentals, SI, 34.1-34.28

[13] http://www.thermalanalysispartners.com/coildesigner.php

[14] ASHRAE, 2001, ASHRAE Handbook-Fundamentals, SI, 14.19

[15] ASHRAE, 2001, ASHRAE Handbook-Fundamentals, 2.2

[16] ASME, Fluid Meters and Their Applications, Eqn. II-III-42, page 220

[17] http://www.heatcraftrpd.com/resources/wiringdiagrams/H-IM-77C.pdf

[18] http://www.thermalanalysispartners.com/xprops.php

[19] ASHRAE, 2001, ASHRAE Handbook-Fundamentals, SI, 6

[20] W.-M. Yan, H.-Y. Lee, Y.-L. Tsay: Thermofluid characteristics of frosted finned tube heat exchangers, International Journal of Heat and Mass Transfer 48, 2005, pp.3073-3080

[21] D.-K. Yang, K.-S. Lee: Frost Formation on a cold plate under turbulent flow, International Journal of Refrigeration 29, 2006, pp.164 – 169

[22] J. Iragorry, Y. Tao, Shaobo Jia: Review Article:A Critical Review of Properties and Models for Frost Formation Analysis, HVAC&R Research, Volume 10, Number 4, October 2004